Article

Immunity

Enzymatic Activity of HPGD in Treg Cells Suppresses Tconv Cells to Maintain Adipose Tissue Homeostasis and Prevent Metabolic Dysfunction

Graphical Abstract

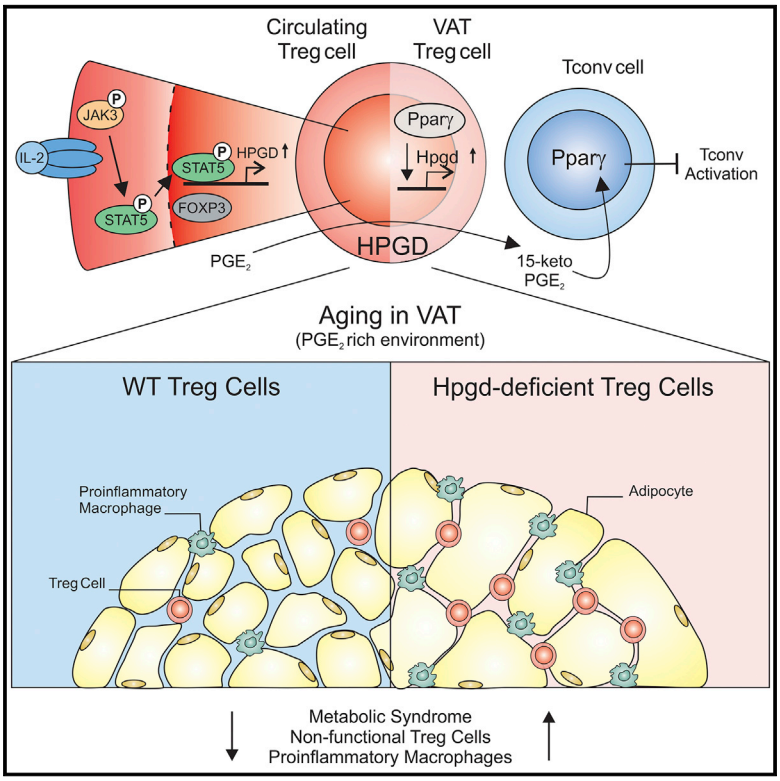

Highlights

- HPGD is specifically upregulated in Treg cells and confers suppressive capabilities
- HPGD-induced Tconv cell suppression is in part mediated by PPARγ signaling
- HPGD expression in Treg cells is vital for VAT homeostasis and metabolic regulation
- T2D patients have a reduced Treg cell fraction expressing lower amounts of HPGD

Authors

Lisa Schmidleithner, Yasser Thabet, Eva Schönfeld, ..., Simon C. Barry, Joachim L. Schultze, Marc Beyer

Correspondence

marc.beyer@dzne.de

In Brief

Regulatory T (Treg) cells are important for preventing autoimmunity and maintaining tissue homeostasis. Schmidleithner et al. report a hydroxyprostaglandin dehydrogenase (HPGD)-mediated tissue- and context-dependent suppressor mechanism used by Treg cells to maintain adipose tissue homeostasis through the metabolism of PGE_2 into the PPARγ ligand 15-keto-PGE2, which is conserved in human and mouse.

Schmidleithner et al., 2019, Immunity *50*, 1232–1248
May 21, 2019
https://doi.org/10.1016/j.immuni.2019.03.014

CellPress

CellPress

Immunity
Article

Enzymatic Activity of HPGD in Treg Cells Suppresses Tconv Cells to Maintain Adipose Tissue Homeostasis and Prevent Metabolic Dysfunction

Lisa Schmidleithner,[1,2,17] Yasser Thabet,[2,17] Eva Schönfeld,[2,17] Maren Köhne,[1,2] Daniel Sommer,[2] Zeinab Abdullah,[3] Timothy Sadlon,[4] Collins Osei-Sarpong,[1,2] Kotha Subbaramaiah,[5] Francesca Copperi,[6] Kristian Haendler,[2,7] Tamas Varga,[1] Oliver Schanz,[8] Svenja Bourry,[1] Kevin Bassler,[2] Wolfgang Krebs,[2] Annika E. Peters,[2,3] Ann-Kathrin Baumgart,[2,3] Maria Schneeweiss,[2] Kathrin Klee,[2] Susanne V. Schmidt,[2] Simone Nüssing,[2] Jil Sander,[2] Naganari Ohkura,[9] Andreas Waha,[10] Tim Sparwasser,[11] F. Thomas Wunderlich,[12] Irmgard Förster,[8] Thomas Ulas,[2] Heike Weighardt,[8] Shimon Sakaguchi,[9] Alexander Pfeifer,[6] Matthias Blüher,[13] Andrew J. Dannenberg,[5] Nerea Ferreirós,[14] Louis J. Muglia,[15] Claudia Wickenhauser,[16] Simon C. Barry,[4] Joachim L. Schultze,[2,7,17] and Marc Beyer[1,2,7,17,18,*]

[1]Molecular Immunology in Neurodegeneration, German Center for Neurodegenerative Diseases (DZNE), Sigmund-Freud-Str. 27, 53127 Bonn, Germany

[2]LIMES-Institute, Laboratory for Genomics and Immunoregulation, University of Bonn, Carl-Troll-Str. 31, 53115 Bonn, Germany

[3]Institute of Experimental Immunology, University Hospital Bonn, Sigmund-Freud-Str. 25, 53127 Bonn, Germany

[4]Molecular Immunology, Robinson Research Institute, University of Adelaide, Norwich Centre, 55 King William St, North Adelaide, SA 5006, Australia

[5]Department of Medicine, Weill Cornell Medical College, 525 E. 68th Street, New York, NY 10065, USA

[6]Institute of Pharmacology and Toxicology, University of Bonn, 53127 Bonn, Germany

[7]PRECISE, Platform for Single Cell Genomics and Epigenomics at the German Center for Neurodegenerative Diseases and the University of Bonn, Sigmund-Freud-Str. 27, 53127 Bonn, Germany

[8]LIMES-Institute, Immunology & Environment, University of Bonn, Carl-Troll-Str. 31, 53115 Bonn, Germany

[9]Laboratory of Experimental Immunology, WPI Immunology Frontier Research Center, Osaka University, Osaka, Japan

[10]Department of Neuropathology, University Hospital Bonn, Sigmund-Freud-Str. 25, 53127 Bonn, Germany

[11]Institute for Medical Microbiology and Hygiene (IMMH), Johannes Gutenberg-University Mainz, Obere Zahlbacherstr. 67, 55131 Mainz, Germany

[12]Max Planck Institute for Metabolism Research, Center for Endocrinology, Diabetes and Preventive Medicine (CEDP), Gleueler Str. 50, 50931 Cologne, Germany

[13]Department of Medicine, University of Leipzig, Liebigstraße 20, 04103 Leipzig, Germany

[14]Pharmazentrum Frankfurt/ZAFES, Institute of Clinical Pharmacology, Goethe-University Frankfurt, Theodor Stern Kai 7, 60590 Frankfurt am Main, Germany

[15]Cincinnati Children's Hospital Medical Center, and Department of Pediatrics, University of Cincinnati College of Medicine, Cincinnati, OH, USA

[16]Institute for Pathology, Martin-Luther University Halle - Wittenberg, Magdeburger Str. 14, 06112 Halle (Saale), Germany

[17]These authors contributed equally

[18]Lead Contact

*Correspondence: marc.beyer@dzne.de

https://doi.org/10.1016/j.immuni.2019.03.014

SUMMARY

Regulatory T cells (Treg cells) are important for preventing autoimmunity and maintaining tissue homeostasis, but whether Treg cells can adopt tissue- or immune-context-specific suppressive mechanisms is unclear. Here, we found that the enzyme hydroxyprostaglandin dehydrogenase (HPGD), which catabolizes prostaglandin E_2 (PGE_2) into the metabolite 15-keto PGE_2, was highly expressed in Treg cells, particularly those in visceral adipose tissue (VAT). Nuclear receptor peroxisome proliferator-activated receptor-γ (PPARγ)-induced HPGD expression in VAT Treg cells, and consequential Treg-cell-mediated generation of 15-keto PGE_2 suppressed conventional T cell activation and proliferation. Conditional deletion of Hpgd in mouse Treg cells resulted in the accumulation of functionally impaired Treg cells specifically in VAT, causing local inflammation and systemic insulin resistance. Consistent with this mechanism, humans with type 2 diabetes showed decreased HPGD expression in Treg cells. These data indicate that HPGD-mediated suppression is a tissue- and context-dependent suppressive mechanism used by Treg cells to maintain adipose tissue homeostasis.

INTRODUCTION

Regulatory T cells (Treg cells) are essential for immune homeostasis by suppressing auto-reactive T cells and fine-tuning immune responses (Josefowicz et al., 2012). Treg cells exert their regulatory function through multiple independent mechanisms

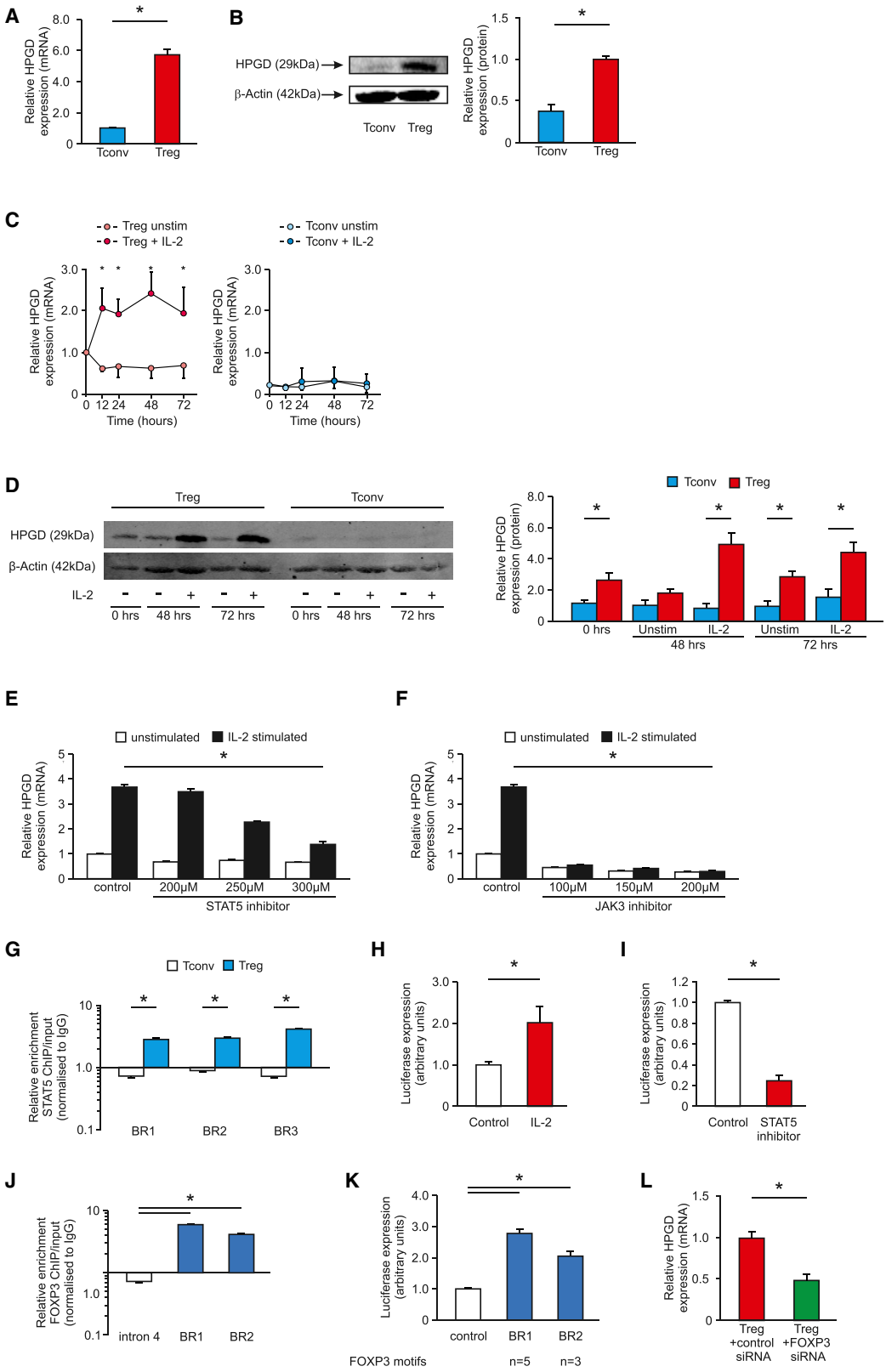

Figure 1. Elevated HPGD Expression in Human Treg Cells Is Dependent on STAT5 and FOXP3

(A) HPGD mRNA expression in human Treg and Tconv cells.

(B) Immunoblotting (left) for HPGD (top) and β-actin (bottom) in human Treg and Tconv cells and densitometric analysis (right).

(legend continued on next page)

(Vignali, 2008). What remains elusive, however, is how these processes interact, what governs the selective use of one mechanism over another, and whether Treg cells can adopt tissue- or immune-context-specific suppressive mechanisms. Supporting the concept of tissue-specific regulation of Treg cell function, several gene expression studies have identified, in addition to a common Treg cell signature (Hill et al., 2007), distinct gene expression patterns associated with Treg cell populations in the spleen and lymph nodes (Hill et al., 2007) compared with tissue-resident Treg cells, such as skeletal muscle Treg cells (Burzyn et al., 2013) or visceral adipose tissue (VAT) Treg cells (Cipolletta et al., 2015; Feuerer et al., 2009). However, it remains to be formally proven whether tissue- and context-specific gene expression in Treg cells is indeed reflected in the usage of tissue-specific suppressive mechanisms by these cells *in vivo*.

It has become clear that tissue-resident Treg cells represent a specific pool of Treg cells that colonize tissues early in life and maintain themselves over the long term (Kolodin et al., 2015). Here, they play a role in both mediating tolerance and tissue repair. It has also been suggested that Treg cells get depleted over time under metabolic challenges, e.g., high-fat diet (HFD) (Feuerer et al., 2009), and that Treg cell transfer under HFD prevents the development of insulin resistance (Deng et al., 2017), although genetic prevention of peroxisome proliferator-activated receptor-γ (PPARγ)-mediated development of VAT Treg cells seems to foster the establishment of a metabolic syndrome (Bapat et al., 2015).

Prostaglandin E_2 (PGE_2) has been described as an important factor contributing to tissue homeostasis in VAT, and abundant levels of PGE_2 in inflammation and cancer progression influence differentiation and effector function of myeloid cells as well as T cells (Kalinski, 2012). Although in myeloid cells, PGE_2 signaling results in the induction of anti-inflammatory programs, the effect of PGE_2 on $CD4^+$ T cells is less clear. *In vitro* data suggest that PGE_2 interferes with proximal T cell receptor signaling (Chemnitz et al., 2006). *In vivo*, however, PGE_2 signaling in naive $CD4^+$ T cells is associated with an expansion of helper T (Th) 1 cells under Th1-promoting conditions (Yao et al., 2009), as well as an enhancement of Th17 differentiation (Boniface et al., 2009). Although Treg cells accumulate in PGE_2-rich environments (Sharma et al., 2005), there is little known about the effect of PGE_2 on Treg cells and the molecular mechanisms by which PGE_2 levels contribute to Treg cell function.

HPGD is the key enzyme for metabolizing PGE_2 into 15-keto-PGE_2 by catalyzing the NAD(+)-linked oxidation of the 15 (S)-hydroxyl group of PGE_2 (Tai et al., 2006). HPGD expression is systemically important, as it is critical for reproduction (Tai et al., 2006), and the loss of HPGD results in primary hypertrophic osteoarthropathy (Uppal et al., 2008), pre-term birth (Roizen et al., 2008), and a patent ductus arteriosus (Coggins et al., 2002). Furthermore, a link between reduced HPGD expression, cell dysplasia, cancer formation, and progression has been established (Myung et al., 2006). Conversely, following liver injury, inhibition of HPGD can promote tissue regeneration (Zhang et al., 2015). In the immune system, however, the role of HPGD has not been well characterized. It has been reported that HPGD is expressed in human monocytes (Maddox and Serhan, 1996), and decreased expression has been observed in tumor-infiltrating macrophages (Eruslanov et al., 2009), but its expression and function in peripheral T cells, particularly in Treg cells, has not been determined. Here, we identified 15-hydroxyprostaglandin dehydrogenase (HPGD) as highly upregulated in Treg cells compared with conventional T (Tconv) cells, indicating that HPGD may be involved in Treg cell function in prostaglandin-rich environments. Our findings clarified the regulation of HPGD expression in Treg cells at the molecular level and showed *in vivo* that HPGD expression is an essential and critical mechanism for tissue homeostasis by augmenting Treg cell suppressive function in environments rich in PGE_2, particularly in VAT.

RESULTS

Human Treg Cells Express High Levels of HPGD

Using transcriptome data from human resting or activated Tconv and Treg cells, we identified 25 genes co-regulated with FOXP3 (Table S1; STAR Methods). Like FOXP3, HPGD showed a high expression difference between Treg and Tconv cells (Figure S1A), which we corroborated in independent samples by qRT-PCR (Figure 1A) and immunoblotting (Figure 1B), with human naive and memory Treg cells expressing similar levels of

(C) Time course of relative HPGD mRNA expression in human Treg and Tconv cells in the presence of IL-2.
(D) Immunoblotting for HPGD (top) and β-actin (bottom) in human Treg and Tconv cells after isolation (0 h) or cultivated for 48 or 72 h without stimulation (unstim) or stimulated with IL-2 (left) and densitometric analysis (right).
(E and F) Relative HPGD mRNA expression in unstimulated or IL-2-stimulated human Treg cells cultured for 24 h in the presence of DMSO (control) or increasing doses of a STAT5 inhibitor (E) or JAK3 inhibitor (F).
(G) ChIP qPCR analysis of human IL-2-stimulated Treg and Tconv cells with a STAT5-specific antibody. Relative enrichment of STAT5 ChIP over input normalized to immunoglobulin G (IgG) is shown.
(H and I) IL-2- and STAT5-dependent activation of luciferase reporter constructs. (H) IL-2-induced HPGD promoter activity. (I) STAT5-dependent HPGD induction.
(J) ChIP qPCR analysis of human expanded cord blood Treg cells with a FOXP3-specific antibody. Relative enrichment of FOXP3 ChIP over input normalized to IgG was calculated. A region within intron 4 was used as a negative control.
(K) Luciferase assay of FOXP3 binding to the respective BRs at the *HPGD* locus. Numbers indicate Foxp3-binding motifs within each region.
(L) Relative HPGD mRNA expression in human Treg cells after silencing of FOXP3. Treg cells were transfected and cultivated for 48 h without stimulation.
(A, B, G, J, and L) *$p < 0.05$ (paired Student's t test); (C) *$p < 0.05$ (two-way ANOVA with false-discovery rate [FDR]); (D–F) *$p < 0.05$ (one-way ANOVA with FDR); (H) *$p < 0.05$ (Mann-Whitney U test); (I and K) *$p < 0.05$ (unpaired Student's t test). Data are representative of fourteen experiments (A; mean and SEM), six experiments (B; mean and SEM), two to five experiments (L; mean and SEM), four experiments (C–F; mean and SEM), three experiments (G and J; mean and SEM), each with cells derived from a different donor. (H, I, and K) Data are from one representative experiment of three (mean and SEM of at least triplicate wells). See also Figure S1 and Tables S1 and S2.

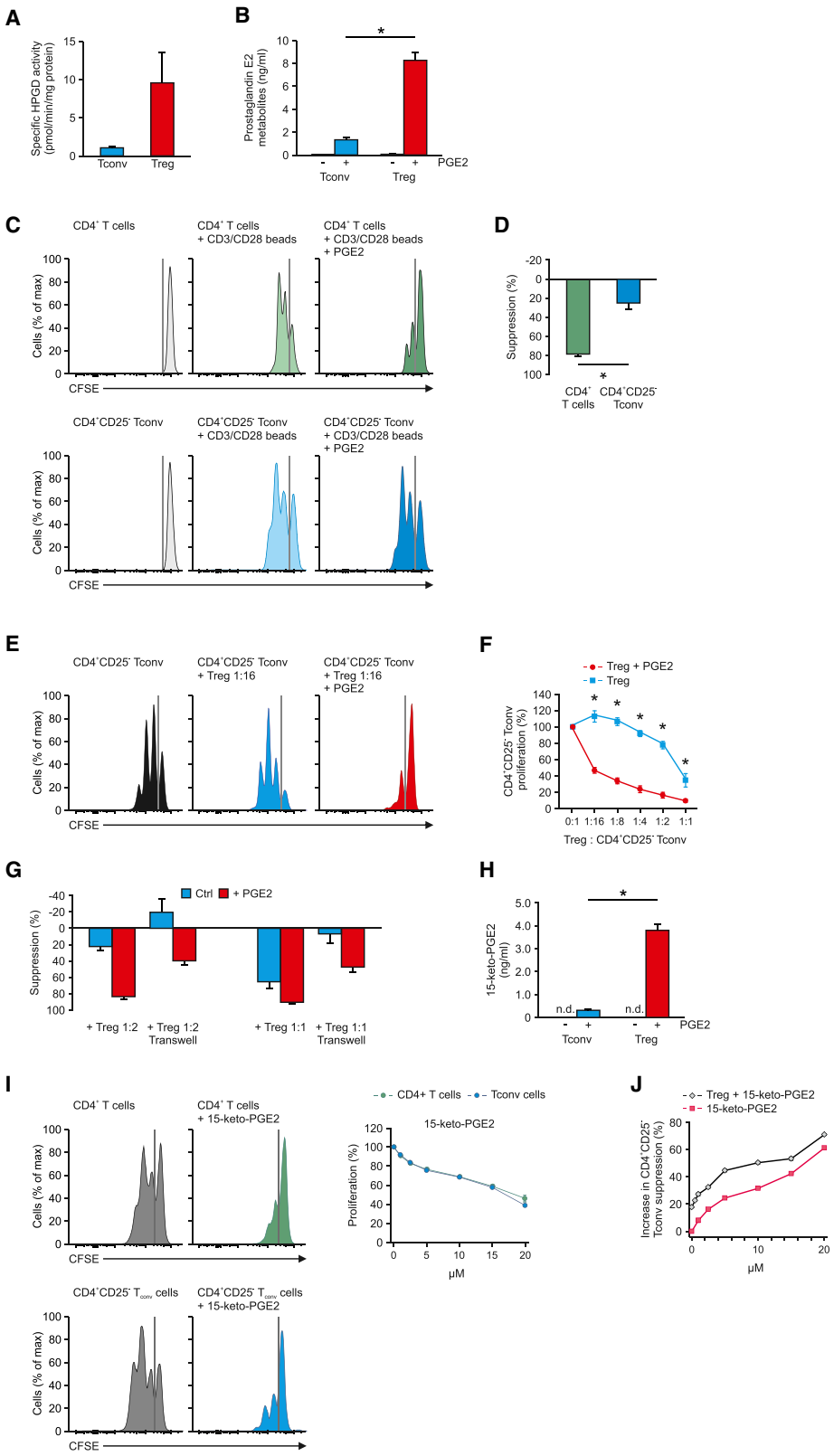

Figure 2. Increased Suppressive Activity of Human Treg Cells Occurs through HPGD-Dependent Metabolism of PGE_2 into 15-keto PGE_2

(A) Specific enzymatic activity of HPGD in lysates from Treg and Tconv cells stimulated with IL-2.

(B) Accumulation of PGE_2 metabolites in the supernatants of Tconv and Treg cells was assessed by enzyme immunoassay (EIA).

(legend continued on next page)

HPGD (Figure S1B). iTregs and other Th subsets (Figure S1C), as well as other immune cell types, showed low levels of HPGD (Figure S1D). In contrast, the HPGD expression level in Treg cells approached the levels detected in myeloid cells, previously reported to specifically express HPGD (Figure S1E; Table S2; Maddox and Serhan, 1996). HPGD was maintained in expanded Treg cells derived from naive and memory Treg cells, suggesting HPGD expression was stable in Treg cells (Figure S1F). Taken together, Treg cells expressed significantly higher levels of HPGD than all other $CD4^+$ T cells.

IL-2 Upregulates HPGD Expression in Treg Cells via STAT5

As interleukin-2 (IL-2) is an essential cytokine for Treg cell survival, activation, and expansion (Malek et al., 2002), we next examined the influence of IL-2 on HPGD expression. Stimulating Treg and Tconv cells with different combinations of IL-2, CD3-mediated T cell receptor stimulation (CD3), and CD28-mediated costimulation (CD28) revealed an IL-2-dependent upregulation of HPGD in Treg cells, but not in Tconv cells, iTregs, and other Th subsets (Figure S1G; data not shown). Upregulation of HPGD mRNA in response to IL-2 reached a plateau at the 12-h time point (Figure 1C). This increase in HPGD mRNA resulted in a significant upregulation in HPGD protein expression (Figure 1D). PGE_2, the main substrate for HPGD, had little effect on HPGD expression levels in Treg cells (Figure S1H), suggesting that HPGD expression in Treg cells was stable even in PGE_2-rich environments.

IL-2 induces signaling in Treg cells via two distinct pathways: the Janus kinase 3 (JAK3)-signal transducer and activator of transcription 5 (STAT5) pathway and the mitogen-activated protein kinase (MAPK) signaling pathway. Blockade of JAK3-STAT5 inhibited the IL-2-mediated upregulation of HPGD (Figures 1E and 1F), and inhibition of MAPK/ERK kinase (MEK) as an inducer of MAPK signaling had no effect (Figure S1I), indicating that HPGD was a downstream target of the IL-2-JAK3-STAT5 signaling pathway.

Next, we demonstrated binding of STAT5 to 3 potential binding regions (BRs) at the *HPGD* locus identified by bioinformatic *in silico* prediction (Figure S1J) by chromatin immunoprecipitation (ChIP)-qPCR (Figure 1G). Binding to BR1 also resulted in increased luciferase activity after IL-2 stimulation in reporter assays (Figure 1H), which could be blocked by inhibition of STAT5 (Figure 1I). In summary, these data established that the IL-2-mediated upregulation of HPGD in human Treg cells was dependent on JAK3-STAT5 signaling through binding of STAT5 to the *HPGD* locus.

Regulation of HPGD Expression in Human Treg Cells Occurs in Part via FOXP3 Binding to the *HPGD* Locus

As HPGD showed co-regulation with FOXP3, we tested whether FOXP3 binds to the genomic *HPGD* locus. By bioinformatic *in silico* prediction, we identified 3 BRs (BR(−15kb), BR1, and BR2) for experimental validation (Figure S1K). Using electrophoretic mobility shift assays (EMSAs) for an enhancer element −15 kb upstream of the transcriptional start site (Figures S1L and S1M) or ChIP-qPCR for two BRs in the promoter region of *HPGD* (Figure 1J), we validated specific FOXP3 binding to the genomic *HPGD* locus. To confirm functional effects of FOXP3 binding to the *HPGD* locus, we performed luciferase reporter assays with BR1 and BR2 and could demonstrate increased reporter activity (Figure 1K), indicating that FOXP3 binding induced HPGD transcription. Furthermore, silencing FOXP3 in human Treg cells resulted in a significant decrease in HPGD expression (Figure 1L), supporting the observation that FOXP3 was critical for the expression of HPGD in Treg cells.

Next, we assessed whether epigenetic mechanisms contributed to the differential regulation of HPGD in human Treg and Tconv cells. Analysis of DNA methylation of a CpG-rich site upstream of exon 1 in the promoter region of the *HPGD* locus (Figure S1N) and analysis of permissive and repressive histone modifications in Treg and Tconv cells (Figures S1O and S1P) both revealed similar permissive epigenetic patterns between Treg and Tconv cells, which in combination with an increase in H3K36me1, which is associated with active transcription (Wagner and Carpenter, 2012), reflective of the higher expression in human Treg cells, supported a mainly transcription-factor-mediated regulation of HPGD expression in Treg cells.

Enzymatic Activity of HPGD Confers Enhanced Suppressive Capacity to Treg Cells

To assess the enzymatic activity of HPGD, we measured its ability to metabolize PGE_2. HPGD enzymatic activity (Figure 2A) as well as production and release of PGE_2 metabolites (Figure 2B) were significantly higher in Treg cells, clearly indicating that HPGD was enzymatically active in human Treg cells.

PGE_2 has been previously described to suppress the proliferation of $CD4^+$ T cells *in vitro* (Chemnitz et al., 2006). Indeed, PGE_2 significantly reduced the proliferation of activated $CD4^+$ T cells in a dose-dependent manner (Figures 2C, 2D, and S2A), which was

(C and D) Effect of PGE_2 on the proliferation of carboxyfluorescein succinimidyl ester (CFSE)-labeled $CD4^+$ T cells compared to $CD4^+CD25^-$ Tconv cells cultured with CD3-CD28-anti-MHC-I-coated beads in the presence of PGE_2 for 72 h (C) and as percent inhibited $CD4^+$ T cells or $CD4^+CD25^-$ Tconv cells (D).

(E and F) Suppression of $CD4^+CD25^-$ Tconv cells by human Treg cells cultured with Treg cells at a ratio of 1:16 with PGE_2 (E) and as a percentage of proliferating $CD4^+CD25^-$ Tconv cells versus the Treg cell/$CD4^+CD25^-$ Tconv cell ratio (F).

(G) Transwell suppression assay of Treg cells co-cultured with PGE_2. Suppression of CFSE-labeled Tconv cells stimulated with CD3-CD28-anti-MHC-I-coated beads.

(H) Accumulation of 15-keto-PGE_2 in the supernatants of Tconv and Treg cells was assessed by LC-MS/MS.

(I) Proliferation of CFSE-labeled $CD4^+$ T cells or $CD4^+CD25^-$ Tconv cells cultured with increasing doses of 15-keto-PGE_2 for 72 h (left) and as percent proliferation (right).

(J) Increased suppression of proliferation of $CD4^+CD25^-$ Tconv cells cultured with increasing doses of 15-keto-PGE_2 in the presence or absence of human Treg cells.

(B, G, and H) *$p < 0.05$ (one-way ANOVA with FDR); (D) *$p < 0.05$ (unpaired Student's t test); (F, I, and J) *$p < 0.05$ (two-way ANOVA with FDR). Data are representative of two experiments (A; mean and SEM), three experiments (B, H, and I; mean and SEM), at least three experiments (G and J; mean and SEM), and at least five experiments (C–F; mean and SEM), each with cells derived from a different donor. See also Figure S2.

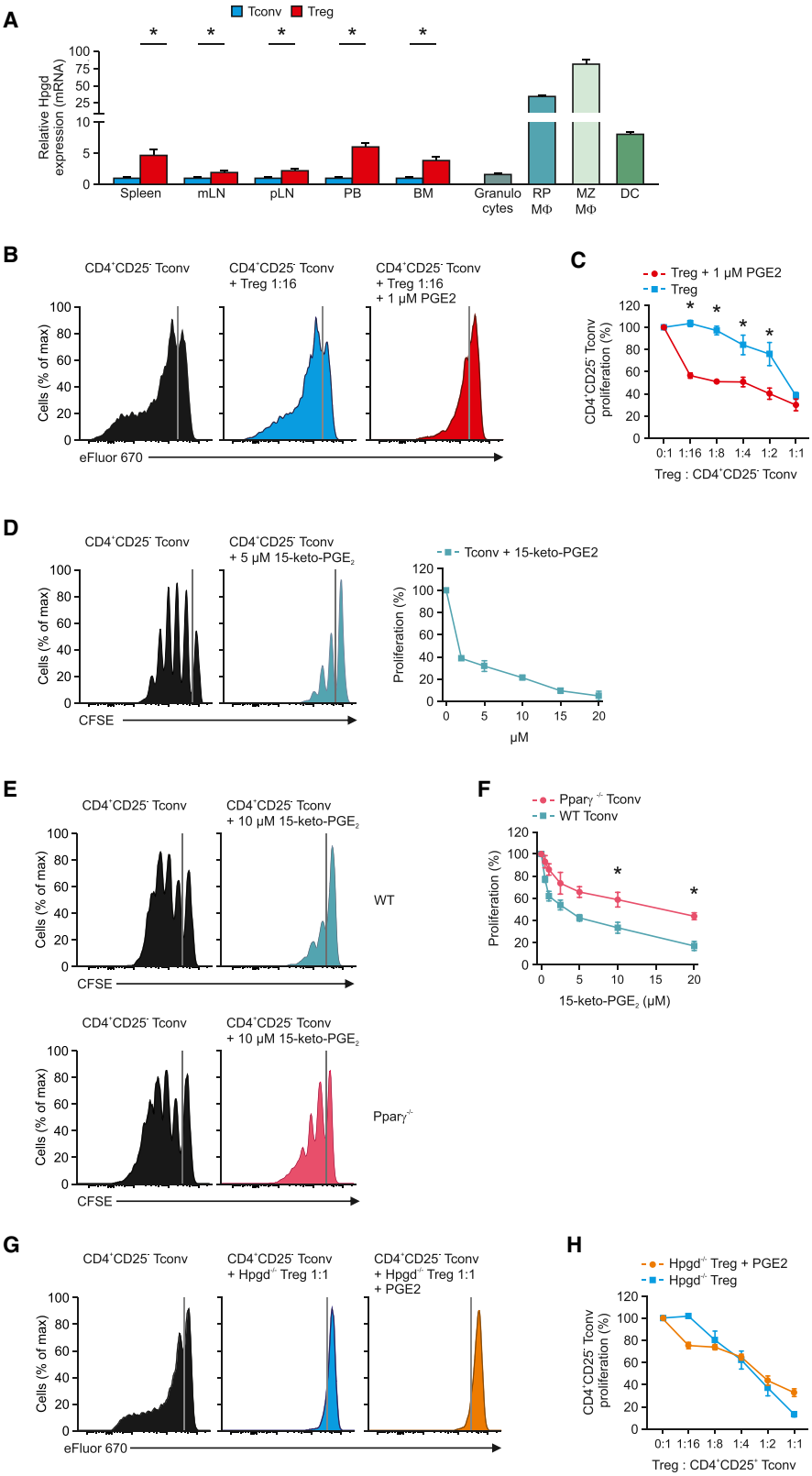

Figure 3. Hpgd Is Expressed and Functional in Murine Treg Cells

(A) Relative Hpgd mRNA expression in murine Treg and Tconv cells from spleen, mesenteric lymph nodes (mLNs), peripheral lymph nodes (pLNs), peripheral blood (pB), bone marrow (BM), granulocytes, marginal zone (MZ) and red pulp (RP) macrophages, as well as splenic dendritic cells (DCs).

(legend continued on next page)

abrogated when Treg-cell-depleted $CD4^+$ T cells were used (Figures 2C and 2D), indicating that the suppressive effect of PGE_2 is mediated by Treg cells. However, when suppressive function was assessed in the presence of PGE_2 during co-culture of Treg and Tconv cells (Figures 2E and 2F), we observed an increase in suppressive function, even at low ratios of Treg versus Tconv cells. This increase was dose dependent, as Treg cells showed even higher suppressive activity when increasing doses of PGE_2 were used (Figure S2B) and restricted to PGE_2 because other prostanoids did not increase the suppressive activity of Treg cells (Figure S2C). Pre-incubation of Treg cells for either 24 or 72 h with PGE_2 resulted in comparable suppressive function to control-treated Treg cells (Figure S2D; data not shown), suggesting that PGE_2 cannot activate Treg cells via PGE_2 receptors (EP receptors) to become more suppressive. Dissecting soluble from cell-surface-mediated suppressive mechanisms by using a Transwell system clearly revealed that PGE_2 enables Treg cells to secrete soluble factors—most likely PGE_2 metabolites—that exert the suppressive effect (Figure 2G). Using liquid chromatography-tandem mass spectrometry (LC-MS/MS), we detected elevated levels of the immediate metabolite of PGE_2 generated by HPGD, 15-keto-PGE_2, in the supernatants of Treg cells exposed to PGE_2 (Figure 2H). Incubation of either $CD4^+$ T cells or $CD4^+CD25^-$ Tconv cells with increasing concentrations of 15-keto-PGE_2 led to a dose-dependent inhibition of proliferation, strongly suggesting that 15-keto-PGE_2 can exert a suppressive effect independent of Treg cell contact (Figure 2I), further supported by a similar dose-dependent increase in suppression of Tconv cells independent of the presence of Treg cells (Figure 2J). Furthermore, addition of 15-keto-PGE_2 had similar enhancing effects on Treg-cell-mediated suppression of Tconv cells when compared with PGE_2 addition (Figure S2E). Taken together, these data clearly suggested that the increased suppressive activity of Treg cells in the presence of PGE_2 was mediated by the soluble metabolite 15-keto-PGE_2.

Further support for 15-keto-PGE_2 being responsible for the observed suppressive effect came from the following observations: first, assessing expression of genes involved in prostanoid and arachidonic acid metabolism showed that HPGD was by far the most significantly elevated gene in Treg cells (Figure S2F), and other enzymes, particularly the two enzymes PTGR1 and PTGR2, responsible for further metabolism of 15-keto-PGE_2, either showed no (PTGR1) or low (PTGR2) expression in T cells (Figures S2F–S2H). Second, incubation of Tconv or Treg cells with 15-keto-PGE_2 did not lead to conversion into PGE_2, strongly supporting unidirectionality of the HPGD-mediated metabolism from PGE_2 to 15-keto-PGE_2 in Treg cells (Figure S2I). Collectively, these data favor a model of HPGD being a major modulator of Treg cell function by converting PGE_2 to the Tconv-cell-suppressive metabolite 15-keto-PGE_2.

Expression of Functional Hpgd in Mouse Treg Cells Induces Pparγ-Mediated Suppression in Tconv Cells

To address whether HPGD expression is conserved between human and murine Treg cells, we analyzed Hpgd expression in murine T cells. Significantly higher Hpgd expression was observed in Treg cells isolated from spleen, mesenteric (mLN) and peripheral lymph nodes, peripheral blood (pB), and bone marrow compared with Tconv cells (Figure 3A). Although, Hpgd expression in Treg cells was relatively low in comparison with splenic myeloid cells (Figure 3A), similar to humans, expression of the of 15-keto-PGE_2-metabolizing enzyme, Ptgr1, is not detectable in murine Treg cells and was only detectable in myeloid and other non-Treg cells (Figure S3A; Table S3), although Ptgr2 was more widely expressed (Figure S3B).

To determine whether PGE_2 also plays a role in murine Treg cell biology, we isolated Treg cells and performed *in vitro* suppression assays (Figures 3B and 3C) with the addition of PGE_2, resulting in significantly increased suppressive activity. To assess whether this effect is likely due to Hpgd-catalyzed conversion of PGE_2 to 15-keto-PGE_2, we stimulated Tconv cells in the presence of 15-keto-PGE_2 and observed a dose-dependent inhibition of Tconv cell proliferation (Figure 3D). Consequently, HPGD-induced metabolism of PGE_2 into the suppressive metabolite 15-keto PGE_2 by Treg cells is a conserved suppressive mechanism between mice and humans.

Accumulation of 15-keto-PGE_2 has been associated with activation of Pparγ (Harmon et al., 2010), a finding we could verify by testing Pparγ target gene expression in adipocytes and bone-marrow-derived macrophages (Figures S3C and S3D). We asked whether the inhibitory effect exerted by Treg-cell-derived 15-keto-PGE_2 is mediated through Pparγ activity. To verify this hypothesis, we stimulated Tconv cells from control ($Ppar\gamma^{fl/WT}Cd4^{Cre}$) or $Ppar\gamma^{fl/fl}Cd4^{Cre}$ animals in the presence of 15-keto-PGE_2 (Figures 3E and 3F) and observed significantly higher proliferation in Pparγ-deficient Tconv cells, suggesting that 15-keto-PGE_2-dependent inhibition was at least partially mediated through Pparγ. Activity of 15-keto PGE_2 might not only be limited to Tconv cells, as *in vitro* experiments support the activation of Pparγ downstream processes also in NK, B, and myeloid cells (Figures S3E–S3G).

To further elucidate the role of Hpgd in Treg cells, we crossed mice with a floxed *Hpgd* allele (Roizen et al., 2008) with $Foxp3^{YFP\text{-}Cre}$ mice to specifically delete Hpgd in Treg cells (Figures S3H and S3I) and assessed the suppressive function of Treg cells. In contrast to Hpgd-sufficient Treg cells, the addition

(B and C) Suppression of eFluor-670-labeled $CD4^+CD25^-$ Tconv cells by murine Treg cells at a ratio of 1:16 with PGE_2 presented as eFluor 670 dilution (B) and as a percentage of proliferating $CD4^+CD25^-$ Tconv cells (C).

(D) Proliferation of CSFE-labeled $CD4^+CD25^-$ Tconv cells cultured with CD3-CD28-coated beads and increasing doses of 15-keto-PGE_2 for 72 h (left) and as a percentage of proliferation of Tconv cells (right).

(E and F) Proliferation of CFSE-labeled $CD4^+CD25^-$ Tconv cells from WT and $Ppar\gamma^{fl/fl}Cd4^{Cre}$ mice cultured with CD3-CD28 beads and 10 μM 15-keto-PGE_2 for 72 h presented as CFSE dilution (E) and cumulative data (F).

(G and H) Suppression of eFluor-670-labeled $CD4^+CD25^-$ Tconv cells by Hpgd-deficient Treg cells without (blue) or in the presence of PGE_2 (orange), presented as eFluor 670 dilution (G) or as a percentage of proliferating Tconv cells (H).

(A) *$p < 0.05$ (Mann-Whitney U test); (C and F) *$p < 0.05$ (two-way ANOVA with FDR). Data are representative of three independent experiments (E–H; mean and SEM) or at least four independent experiments (A–D; mean and SEM). See also Figure S3 and Table S3.

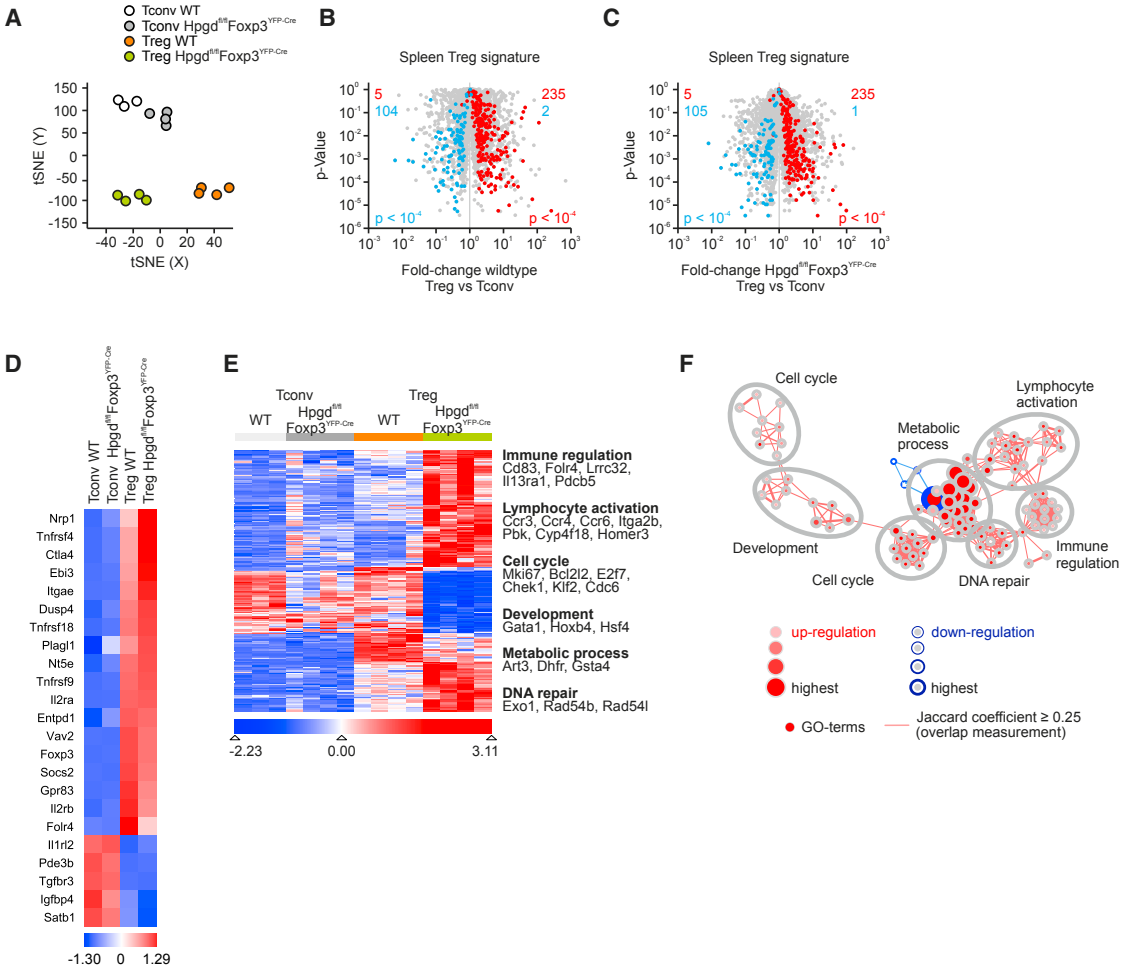

Figure 4. Hpgd-Deficient Treg Cells Retain the Transcriptional Treg Cell Program

Transcriptome analysis of splenic Tconv and Treg cells from WT and *Hpgd*$^{fl/fl}$*Foxp3*$^{YFP-Cre}$ mice.

(A) t-distributed stochastic neighbor embedding (t-SNE) based on expressed and variable genes.

(B and C) Fold-change (FC) versus p value plots comparing transcriptomes of Treg and Tconv isolated from control (B) and *Hpgd*$^{fl/fl}$*Foxp3*$^{YFP-Cre}$ mice (C). The Treg cell signature from Hill et al. (2007) was overlaid onto the plot. p values were generated with the chi-square test.

(D) Heatmap showing the z-transformed expression values of selected genes from the common murine Treg cell core signature, colored from blue to red.

(E) Heatmap of the gene signature identified in Figure S4D. Gene expression values were z transformed for visualization and are colored from blue to red.

(F) Network visualization of Gene Ontology enrichment analysis based on the signature genes using BiNGO and EnrichmentMap. Enriched GO terms are depicted by red nodes, where color and size represent the corresponding FDR-adjusted enrichment p value (q value). Overlap of genes between nodes is indicated by edge thickness.

See also Figure S4 and Table S4.

of PGE_2 to Hpgd-deficient Treg cells did not increase their suppressive activity (Figures 3G and 3H). Taken together, these data suggest that Hpgd expression was necessary for the metabolism of PGE_2 and that the subsequent increase in suppression of T cell activation was mediated through the accumulation of 15-keto PGE_2.

Loss of Hpgd Does Not Alter the Treg-Cell-Associated Phenotype

To further study the impact of Hpgd on Treg cells, we analyzed 6- to 12-week-old male mice and detected no overt differences in Treg cell percentages or numbers (Figures S4A and S4B) or expression of Treg-cell-associated molecules (Figure S4C). To identify differences between wild-type and Hpgd-deficient Treg cells, we performed transcriptome analysis of Tconv and Treg cells isolated from control and *Hpgd*$^{fl/fl}$*Foxp3*$^{YFP-Cre}$ animals. T-distributed stochastic neighbor embedding (t-SNE) of variable genes revealed that Hpgd-deficient Treg cells resembled control Treg cells (Figure 4A). Next, we examined the expression of genes representing the murine Treg cell gene signature (Hill et al., 2007). Superimposition of this signature revealed no significant over- or under-representation of Treg cell signature genes in HPGD-deficient or wild-type (WT) Treg cells (Figures 4B and 4C). Visualization of key genes further demonstrated that Hpgd-deficient Treg cells retained the Treg cell gene signature (Figure 4D). Next, we identified a set of

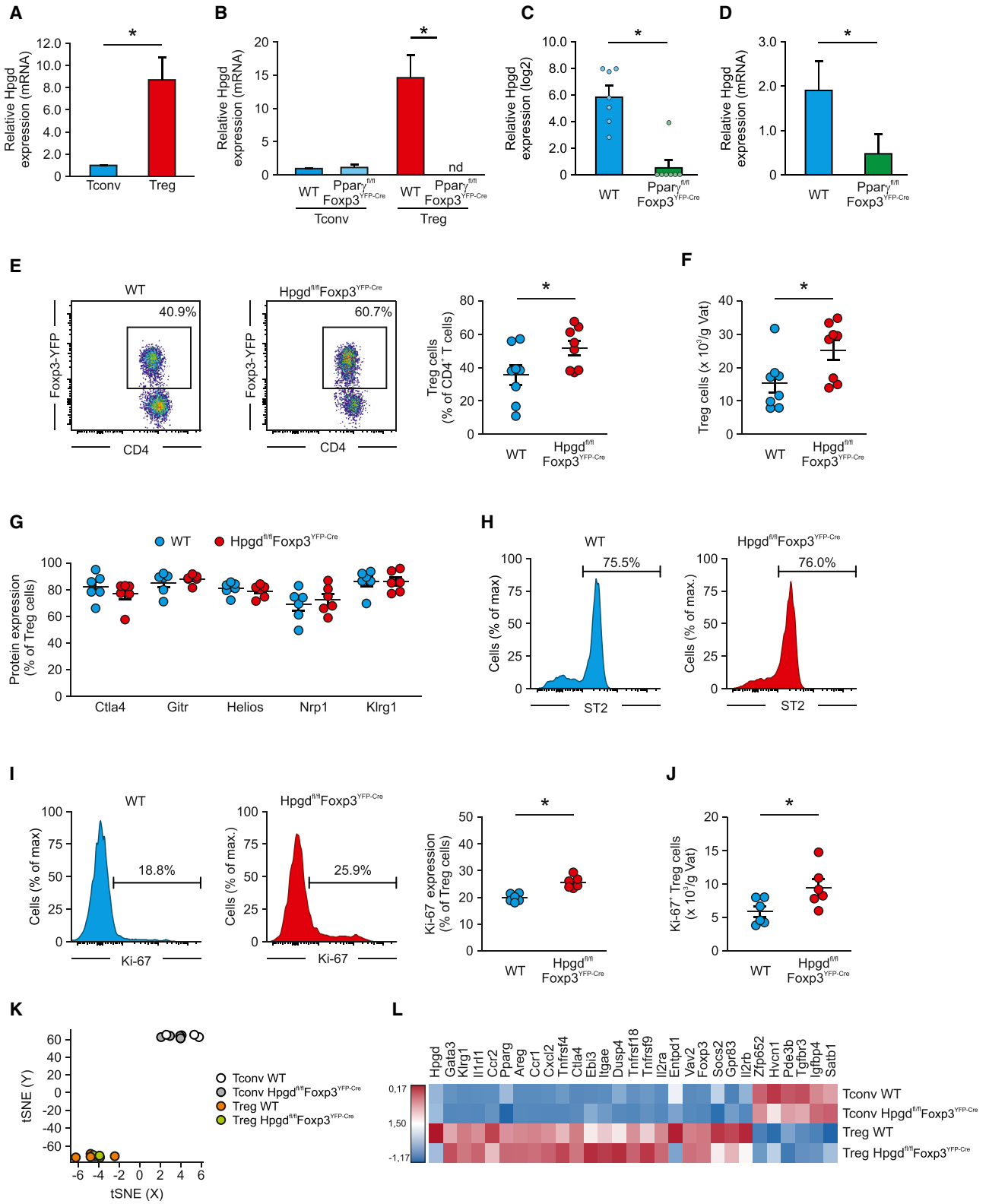

Figure 5. Hpgd-Deficient Treg Cells Accumulate in Visceral Adipose Tissue of Aged Mice

(A) Relative Hpgd mRNA expression in Treg and Tconv cells isolated from visceral adipose tissue by qPCR (n = 6 each).

(B) Relative Hpgd mRNA expression in Treg and Tconv cells isolated from VAT by qPCR from mice harboring Pparγ-deficient and control Treg cells.

(legend continued on next page)

210 genes that were specifically altered in Hpgd-deficient Treg cells (Figures 4E, S4D, and S4E; Table S4). Gene Ontology enrichment analysis (GOEA) followed by network visualization revealed differences in biological processes associated with immune regulation, lymphocyte activation, cell cycle, and DNA repair as well as metabolic processes (Figure 4F). Altogether, the global analysis of Hpgd-deficient Treg cells identified no major changes to the core Foxp3-associated gene expression program.

High Expression of Hpgd in VAT-Associated Treg Cells Is Dependent on Pparγ

In situ, VAT displays some of the highest activity of COX-1 and microsomal prostaglandin E synthase-1 (mPGES-1), which under homeostatic conditions produce PGE_2. Therefore, we analyzed Hpgd expression in Treg cells from VAT of male mice, which revealed highly elevated levels of Hpgd mRNA (Figures 5A and S5A). Increased Hpgd expression was specific to VAT Treg cells, as other tissue-derived Treg cells showed lower Hpgd levels similar to expression levels detected in Treg cells isolated from lymphoid organs (Figure S5B).

As Pparγ is a major driver for the phenotype of VAT-associated Treg cells (Cipolletta et al., 2012), we performed both population-based (Figure 5B) and single-cell qPCR (Figure S5C) on VAT-associated Treg cells from *Pparγ*$^{fl/fl}$*Foxp3*$^{YFP\text{-}Cre}$ and *Pparγ*$^{fl/WT}$*Foxp3*$^{YFP\text{-}Cre}$ animals and observed significantly decreased levels of Hpgd in Pparγ-deficient Treg cells, suggesting that elevated Hpgd expression in VAT-associated Treg cells was dependent upon Pparγ. Recent data support that the Pparγ program is induced already in a VAT Treg cell precursor population in the spleen (Li et al., 2018). Reanalysis of this dataset revealed increased HPGD expression in the Pparγ-expressing Treg cell precursor population (Figure 5C), a finding we could support by analysis of Hpgd expression in splenic Treg cells from *Pparγ*$^{fl/fl}$*Foxp3*$^{YFP\text{-}Cre}$ and *Pparγ*$^{fl/WT}$ *Foxp3*$^{YFP\text{-}Cre}$ animals (Figure 5D). The existence of a destined population of Treg cells instructed to express high levels of Hpgd through Pparγ in conjunction with additional mechanisms, e.g., epigenetic regulation, was further supported by the notion that retroviral expression of Pparγ with Foxp3 in Tconv cells recapitulated much of the VAT-associated Treg cell program but could not induce Hpgd expression (data not shown).

Hpgd Deficiency Results in an Increase in Visceral Adipose Tissue Treg Cells in Aged Mice

It has been reported that the development of pathology associated with a defect in Treg-cell-suppressive activity, if not resulting in an immediate overt scurfy-like phenotype, can take up to 6 months or even longer to manifest (Huynh et al., 2015; Shrestha et al., 2015). Therefore, we characterized splenic Treg cells from aged animals (>40 weeks; Figures S5D–S5I) and, as in young mice, were unable to detect changes in any of the parameters analyzed.

However, when we assessed older animals for VAT Treg cells, we observed a significant increase in both the percentage and numbers of Treg cells in VAT from Hpgd-deficient mice (Figures 5E and 5F), although the expression of Treg-cell-associated markers, including ST2, was unchanged (Figures 5G and 5H). This was accompanied by a higher number of Ki-67-positive VAT Treg cells in Hpgd-deficient mice (Figures 5I and 5J). This increase was specific for VAT, as Treg cells from other organs, including brown adipose tissue (BAT), showed no expansion of Treg cells (Figure S5J). Taken together, these data support an expansion of the pool of Hpgd-deficient Treg cells specific in VAT in aged animals.

To address whether the observed changes in Treg cell numbers were consequences of cell-intrinsic or cell-extrinsic processes, we performed transcriptome analysis of VAT Treg cells from 12-week-old animals before development of potentially influencing pathology. This analysis revealed that Hpgd-deficient and WT Treg cells were highly similar (Figure 5K) with comparable enrichment of the VAT Treg cell signature (Cipolletta et al., 2015; Figures S5K and S5L). Only Hpgd and Entpd1 as key members of the Treg cell gene signature showed a decrease in Hpgd-deficient Treg cells (Figure 5L). In total, 101 genes (Table S5) were differentially expressed between both cell populations (Figure S5M). Correlation of these genes with gene ontology terms revealed no enrichment of any immunologic or metabolic pathways, supporting that the loss of Hpgd had little impact for the core transcriptional program of VAT Treg cells.

To further support that Hpgd-deficient Treg cells showed no defect in competitive fitness, we analyzed heterozygous female *Hpgd*$^{fl/fl}$*Foxp3*$^{YFP\text{-}Cre/WT}$ mice. Due to random X chromosome inactivation, approximately 40%–50% of the Treg cells in these mice are expected to express YFP. When we examined *Hpgd*$^{WT/WT}$*Foxp3*$^{YFP\text{-}Cre/WT}$ heterozygous female

(C) Relative Hpgd expression in splenic Pparγ-positive and negative Treg cells (Li et al., 2018).
(D) Relative Hpgd expression in splenic WT and Pparγ-deficient Treg cells by qPCR.
(E) Representative (left) and cumulative (right) flow cytometric analysis of Ki-67 expression in Hpgd-deficient and Hpgd-competent Treg cells from VAT of aged mice (n = 6 each).
(F) Total numbers of Ki-67$^+$ Hpgd-deficient and Hpgd-competent VAT Treg cells of aged mice (n = 6 each).
(G) Cumulative flow cytometric analysis of Ctla-4, Gitr, Helios, Neuropilin-1 (Nrp1), and Klrg1 from Hpgd-deficient and Hpgd-competent VAT Treg cells of aged mice (n = 6 each).
(H) ST2 expression in Hpgd-deficient and Hpgd-competent VAT Treg cells aged mice.
(I) Representative (left) and cumulative (right) flow cytometric analysis of Ki-67 expression on Hpgd-deficient and Hpgd-competent VAT Treg cells of aged mice (n = 6 each).
(J) Total numbers of Ki-67$^+$ Hpgd-deficient and Hpgd-competent VAT Treg cells of aged mice (n = 6 each).
(K and L) Transcriptome analysis of Tconv and Treg cells from at least four WT and *Hpgd*$^{fl/fl}$*Foxp3*$^{YFP\text{-}Cre}$ mice. t-SNE based on expressed and variable genes (K) and heatmap of Treg cell gene signature (L) are shown.
Data are representative of at least two independent experiments (D–J) with at least six mice, three independent experiments (A, B, and D; mean and SEM), or seven animals per group (C). (A) *p < 0.05 (paired Student's t test); (C–H and J) *p < 0.05 (unpaired Student's t test); (B) *p < 0.05 (one-way ANOVA with FDR). See also Figure S5 and Table S5.

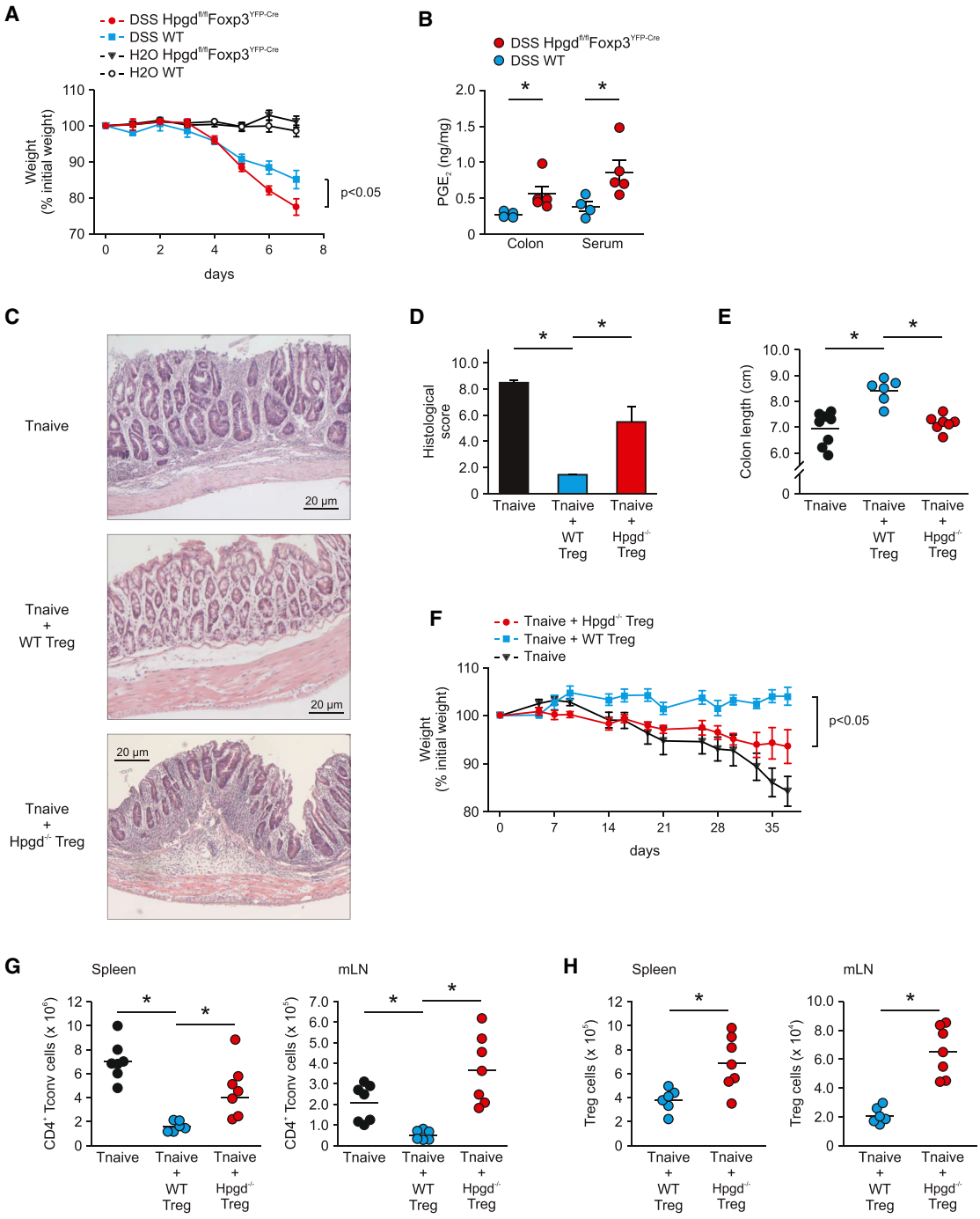

Figure 6. Loss of Hpgd in Treg Cells Results in Reduced Suppressive Function *In Vivo*

(A) Weight loss of male *Hpgd*$^{fl/fl}$*Foxp3*$^{YFP\text{-}Cre}$ and control *Hpgd*$^{fl/WT}$*Foxp3*$^{YFP\text{-}Cre}$ mice that received drinking water containing 5% DSS or water. Data are representative of two experiments (n = 4 each).

(B) Concentration of PGE_2 in colonic tissue (left) and serum (right) from male *Hpgd*$^{fl/fl}$*Foxp3*$^{YFP\text{-}Cre}$ and *Hpgd*$^{fl/WT}$*Foxp3*$^{YFP\text{-}Cre}$ mice (WT) that received drinking water containing 5% DSS for 7 days.

(C) H&E staining of colon sections from *Rag2*$^{-/-}$ mice at 6 weeks after the transfer of $CD4^+CD62L^{hi}$ naive T cells (Tnaive) alone or in combination with HPGD-competent (WT Treg) or HPGD-deficient Treg cells. Original magnification, ×200; scale bars, 20 μm.

(D) Histology scores of colon sections of *Rag2*$^{-/-}$ mice 6 weeks after the transfer in (C).

(E) Colon length of *Rag2*$^{-/-}$ mice 6 weeks after the transfer in (C).

(legend continued on next page)

mice, 20%–30% of the Treg cells showed YFP expression, indicating that the *Foxp3*$^{YFP\text{-}Cre}$ allele confers a slight disadvantage to Treg cells in a competitive setting (Figure S5N). In *Hpgd*$^{fl/fl}$ *Foxp3*$^{YFP\text{-}Cre/WT}$ mice, we found a similar ratio of Hpgd-sufficient Foxp3^{+}YFP^{-} to Hpgd-deficient Foxp3^{+}YFP^{+} Treg cells, which was constant over time (Figure S5O), supporting that Hpgd-deficient Treg cells did not have a competitive disadvantage relative to Hpgd-sufficient Treg cells.

To further assess the competitive fitness of Hpgd-deficient Treg cells, we transferred Hpgd-deficient or WT Treg cells together with naive T cells and Treg cells from *Foxp3*$^{IRES\text{-}RFP}$ mice to *Rag2*$^{-/-}$ animals (Figure S5P). Co-transfer of Treg cells from *Foxp3*$^{IRES\text{-}RFP}$ mice was used to ensure that the impact of Hpgd could be assessed independently of a potential influence caused by the development of colitis (Figure S5Q). We did not observe major differences between Hpgd-deficient and WT Treg cells in mLNs in these animals 8 weeks after transfer (Figures S5R–S5T). Transcriptome analysis of Hpgd-deficient and WT Treg cells from mLNs of these animals revealed no significant alterations between both cell populations (Figures S5U and S5V). Taken together, these data support that the loss of Hpgd resulted in an expansion of VAT Treg cells in aged animals not caused by alterations of the transcriptional program or competitive fitness of Treg cells.

Loss of Hpgd Expression Decreases Treg Cell Function

To assess whether the loss of Hpgd in Treg cells also influenced their suppressive capacity *in vivo*, we used the dextran sulfate sodium (DSS) colitis model. Hpgd-deficient Treg cells were less potent in preventing DSS-induced colitis as evidenced by increased weight loss (Figure 6A) and augmented local and systemic concentrations of PGE_2 as a sign of defective PGE_2 metabolism, although other prostaglandins were unaltered (Figures 6B, S6A, and S6B). Consistently, we found higher cellularity in mLN of *Hpgd*$^{fl/fl}$*Foxp3*$^{YFP\text{-}Cre}$ animals (Figure S6C). Together, these data indicate that the specific loss of Hpgd in Treg cells resulted in reduced regulatory function of Treg cells *in vivo*.

Next, we used the adoptive colitis model, which was characterized by elevated levels of PGE_2 in inflamed tissue and serum (Figures S6D and S6E) to further evaluate the suppressive capacity of Hpgd-deficient Treg cells. Transfer of naive T cells into *Rag2*$^{-/-}$ mice led to the development of colitis, although co-transfer of *Hpgd*$^{fl/WT}$*Foxp3*$^{YFP\text{-}Cre}$ Treg cells prevented colitis-associated pathology (Figures 6C–6H). Co-transfer of Hpgd-deficient Treg cells resulted in colitis-associated pathology and a significant expansion of Tconv cells in spleen and mLN, despite a concomitant increase in Treg cells (Figures 6C–6H), suggesting a functional impairment of Hpgd-deficient Treg cells not caused by lower proliferation or higher apoptosis of Hpgd-deficient Treg cells *in vivo*.

Loss of Hpgd in Treg Cells Results in VAT Inflammation and Development of a Metabolic Syndrome

As Treg cells are critically involved in the homeostasis of VAT and VAT-associated immune cells, we asked whether the increase in Hpgd-deficient Treg cells would influence VAT homeostasis.

We observed a significant increase in VAT-associated macrophages in aged mice (>40 weeks) by immunohistochemistry (Figures 7A and 7B) with a concomitant increase in adipocyte size (Figure 7C). Flow cytometric quantification confirmed the increase of macrophages (Figure 7D), although numbers of granulocytes were unaltered (Figure S7A). Further characterization of macrophages indicated the development of a more pro-inflammatory phenotype (Figures 7E and 7F), which has been associated with altered organ functions, including altered metabolism of VAT (Lumeng et al., 2007). Similarly, VAT inflammation has been associated with increased numbers of natural killer (NK) cells (Wensveen et al., 2015), which we could demonstrate by flow cytometry (Figure 7G), although NKT cells were unaffected (Figure S6B). Although overall and VAT weight was not different in aged animals with Hpgd-deficient Treg cells (Figures S7C and S7D), we observed increased fasting glucose levels (Figure 7H), increased insulin levels (Figure 7I), impaired insulin tolerance (Figure 7J), glucose tolerance (Figure S7E), and homeostasis model assessment-estimated insulin resistance (HOMA-IR) (Figure 7K), which was not caused by altered food and water intake, respiration, or decreased activity (data not shown). In line with insulin resistance in these animals, we observed decreased pAKT/AKT ratios in VAT (Figure 7L) as well as BAT (Figure S7F). This was accompanied by an increase in Ap2 protein expression in VAT (Figure S7G), although Ucp1 expression was not detectable in VAT and unaltered in BAT (data not shown), supporting an impairment in metabolic activity not associated with increased browning of VAT. To demonstrate that this effect was dependent on the accumulation of non-functional Treg cells in aged animals, we analyzed young (6–10 weeks) and middle-aged animals (18–20 weeks) and could not detect any alterations in VAT-associated Treg cell numbers or metabolic parameters (Figures S7H–S7N; data not shown). To determine how this loss of Treg cell functionality would affect the development of HFD-induced inflammation, we determined Treg cell numbers and the metabolic state of HFD-fed animals. Although body weight and fasting glucose were not altered, we observed decreased insulin sensitivity as well as increased numbers of Treg cells in VAT of animals with Hpgd-deficient Treg cells, supporting a similar effect as observed in aged mice also for HFD-fed animals (Figures S7O–S7R). Collectively, these findings suggest that, although Hpgd-deficient Treg cells accumulated in VAT in aging or obesity, they failed to prevent the development of pro-inflammatory macrophages and NK cells, which in turn induced adipose tissue inflammation, subsequently leading to the development of a metabolic syndrome in these mice.

(F) Body weight of *Rag2*$^{-/-}$ mice 6 weeks after the transfer in (C), presented relative to initial body weight.
(G and H) Recovery of Tconv (G) and Treg cells (H) from spleens and mesenteric lymph nodes of *Rag2*$^{-/-}$ mice 6 weeks after the transfer in (C).
(A and F) *$p < 0.05$ (two-way ANOVA with FDR); (B, D, E, and G) *$p < 0.05$ (one-way ANOVA with FDR); (H) *$p < 0.05$ (Mann-Whitney U test). Data are representative of two independent experiments (A) or are pooled from two independent experiments of at least four recipient mice (B; mean and SEM) or at least six recipient mice (C–H; mean and SEM). See also Figure S6.

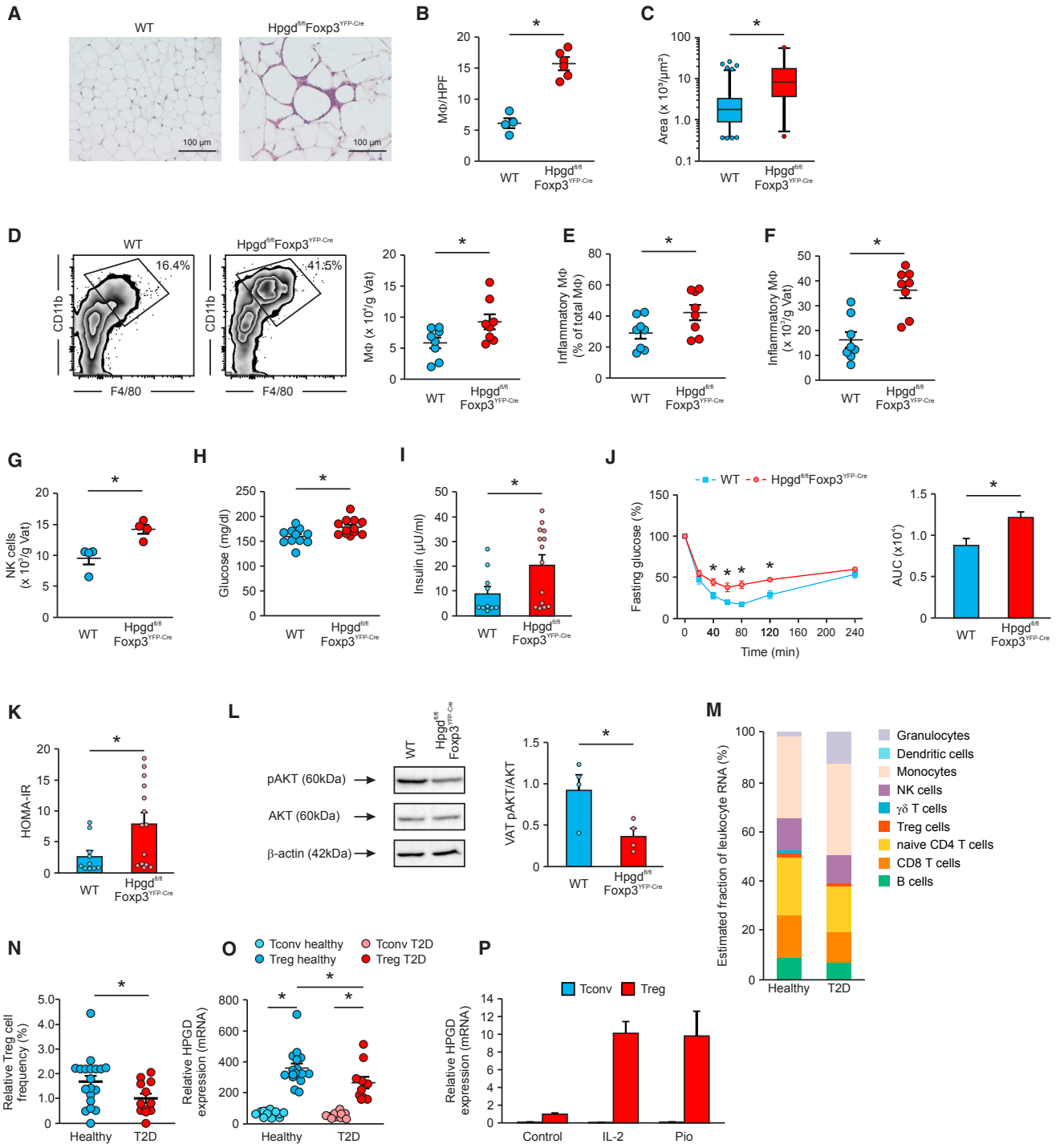

Figure 7. Loss of Hpgd Results in Inflammation in VAT of Aged Mice and Correlated with Metabolic Dysfunction in Mice and Humans

(A) Representative staining of VAT from aged mice with Hpgd-competent (n = 4) or Hpgd-deficient Treg cells (n = 5) with H&E. Original magnification, ×200; scale bars, 100 μm.

(B) Total numbers of macrophages per high power field (HPF) from visceral adipose tissue.

(C) Quantification of adipocyte size.

(D) Representative flow cytometric analysis (left) and total numbers of macrophages from visceral adipose tissue (right) of old mice with Hpgd-deficient and Hpgd-competent Treg cells (n = 8 each).

(E) Cumulative flow cytometric analysis of $CD11b^+F4/80^+CD11c^+$ inflammatory macrophages in visceral adipose tissue of aged mice harboring Hpgd-deficient or Hpgd-competent Treg cells (n = 8 each).

(legend continued on next page)

Type 2 Diabetes in Humans Is Associated with Decreased HPGD Levels in Treg Cells

As the development of a metabolic syndrome has been associated with a loss of Treg cells in murine models (Feuerer et al., 2009), we asked whether we could establish an association between Treg cells, HPGD levels, and development of type 2 diabetes (T2D) in humans.

We focused first on the frequency of Treg cells in pB and applied linear support vector regression (SVR) to pB expression data from two independent cohorts of T2D patients and could establish significantly decreased frequencies of Treg cells in patients with T2D (Figures 7M, 7N, S7S, and S7T). Next, we determined HPGD expression in Treg cells isolated from T2D patients and observed decreased HPGD levels in Treg cells (Figure 7O), although FOXP3 levels were unaffected (Figure S7U), indicating that HPGD expression was specifically downregulated, although the general Treg cell signature was unaffected during the development of T2D. This finding was validated in an independent cohort of T2D patients (Figures S7V and S7W; Ferraro et al., 2014).

As we established Pparγ as a tissue-specific regulator of Hpgd expression in murine Treg cells—which is therapeutically targeted in humans with T2D by PPARγ agonists to counteract insulin resistance—we asked whether this would potentially also affect HPGD expression in Treg cells. Therefore, we incubated human Treg cells with an agonist for PPARγ and observed an increase in HPGD expression (Figure 7P), further underlining the role of PPARγ for the regulation of HPGD expression in Treg cells.

Taken together, our data support that Treg cells in humans were negatively affected in T2D by alterations in numbers and functionality linked to altered HGPD expression, which could be overcome through PPARγ activation positively influencing HPGD levels in Treg cells.

In summary, we have identified a novel HPGD-mediated context- and tissue-specific suppression mechanism important for PGE2-rich environments conserved between humans and mice.

DISCUSSION

Several mechanisms have been implicated in the regulatory function of Treg cells, including the release of suppressive cytokines and cell-contact-dependent suppression (Vignali, 2008). In this report, we identified a key enzyme, HPGD, which contributed to Treg cell function in PGE_2-rich environments. HPGD, the main enzyme responsible for metabolism of PGE_2 into its bioactive metabolite 15-keto-PGE_2, was highly expressed in human and murine Treg cells and acted through the generation of 15-keto-PGE_2, which activated PPARγ in Tconv cells and impacted Tconv cell proliferation. This observation finally resolves the long-standing controversy between the descriptions of PGE_2 as a factor mainly influencing Tconv cell differentiation (Boniface et al., 2009; Yao et al., 2009) and initial reports working with total $CD4^+$ T cell populations observing mainly suppressive effects (Chemnitz et al., 2006). Although it is important to note that additional eicosanoids, leukotrienes, and other prostaglandins play a role in the regulation of T cell function and that high expression of HPGD in myeloid cells could also be an important contributor to the fine-tuning of prostaglandin levels *in vivo*, our data established a clear link between HPGD, PGE_2, and the direct metabolite 15-keto-PGE_2 for Treg cell function. Sole expression of HPGD in Treg cells makes them unique in their propensity to generate 15-keto PGE_2 as a potential signaling molecule, as myeloid cells not only express HPGD but also express PTGR1 and PTGR2, which will result in rapid and unidirectional degradation of PGE_2 into 13,14-dihydro-15-keto-PGE_2.

Induction of HPGD under steady-state conditions was dependent on FOXP3 and constitutive IL-2 signaling, as IL-2 administration was sufficient to increase HPGD levels in human Treg cells in a JAK3-STAT5-dependent manner. However, IL-2 alone was insufficient to induce HPGD expression in Tconv cells, indicating that other factors must contribute to high expression levels of HPGD in Treg cells. One factor we could identify is PPARγ, which is the main driver of the transcriptional signature of VAT-associated Treg cells (Bapat et al., 2015; Cipolletta et al., 2012, 2015). Loss of PPARγ significantly decreased HPGD levels in murine VAT-associated Treg cells, a result consistent with evidence that PPARγ ligands can induce HPGD transcription in other cell types (Subbaramaiah et al., 2012). The dependence of high HPGD levels in Treg cells on PPARγ was already evident in VAT Treg cell precursors in the spleen, yet expression of the combination of IL-2, PPARγ, and FOXP3 was not sufficient to induce HPGD in naive Tconv cells, indicating that an additional factor (or factors) is needed to induce HPGD expression in Treg cells. Such factors may include the global epigenetic landscape in Treg cells and the expression

(F) Total numbers of inflammatory macrophages in VAT of aged mice (n = 8 each).
(G) Total numbers of VAT NK cells of aged mice (n = 8 each).
(H and I) Serum glucose (H) and insulin levels (I) of aged mice harboring Hpgd-competent (n = 11) or Hpgd-deficient Treg cells (n = 12).
(J) (Left) Intraperitoneal insulin tolerance test (ITT) of aged mice harboring Hpgd-deficient or Hpgd-competent Treg cells (n = 4 each). (Right) Calculated area under the curve (AUC) from all mice tested by ITT.
(K) HOMA-IR of aged mice harboring Hpgd-competent (n = 11) or Hpgd-deficient Treg cells (n = 12).
(L) pAKT/AKT ratio in visceral adipose tissue of aged mice with Hpgd-competent or Hpgd-deficient Treg cells (n = 4 each). Immunoblotting (left) for pAKT (top), AKT (middle), and β-actin (bottom) and densitometric analysis to quantify the ratio of pAKT to AKT (right) are shown.
(M) Quantification of leucocyte subsets from healthy individuals (n = 19) and type 2 diabetes patients (T2D) (n = 12) using CIBERSORT (for dataset details, see STAR Methods).
(N) Enumeration of Treg cells in (M).
(O) Relative HPGD mRNA expression by microarray analysis in Tconv and Treg cells isolated from peripheral blood from healthy individuals (n = 12) and patients with T2D (n = 9).
(P) Relative HPGD mRNA expression in human Tconv and Treg cells stimulated for 48 h with IL-2 or pioglitazone (Pio).
(B–L and N) *$p < 0.05$ (unpaired Student's t test); (O) *$p < 0.05$ (one-way ANOVA with FDR); (J) *$p < 0.05$ (two-way ANOVA with FDR). Data are representative of at least two independent experiments. See also Figure S7.

of VAT Treg cell program-shaping transcription factors like IRF4 and BATF (Vasanthakumar et al., 2015); however, IL-33, which critically contributes to the orchestration of adipose-tissue-resident Treg cells does not directly induce HPGD expression (data not shown). Notably, in humans, pharmacological activation of PPARγ could upregulate HPGD expression in Treg cells, supporting the idea that HPGD could be a pharmacological target in Treg cells.

This could be of particular importance, as the loss of HPGD in Treg cells resulted in decreased functionality of Treg cells. Moreover, mice with Hpgd-deficient Treg cells, when aged over 40 weeks, spontaneously developed a metabolic syndrome despite an expansion of visceral adipose tissue Treg cells. Mechanistically, this can be explained by the fact that adipose tissue is rich in PGE_2 under homeostatic conditions and contains a distinct Treg cell population that expresses high levels of Hpgd. Under homeostatic conditions, these Treg cells are required to prevent VAT inflammation. Over time, the loss of Hpgd-mediated functionality results in increased local inflammation associated with increased numbers of inflammatory macrophages and NK cells. Despite the increase in the proliferation of local VAT-associated Treg cells, this ultimately leads to a breakdown of tissue homeostasis, the development of insulin resistance, and a metabolic syndrome.

The observation that loss of Hpgd in Treg cells results in the development of insulin resistance in aged male animals led us to also analyze HPGD expression in Treg cells from patients with type 2 diabetes. In addition to data indicating decreased Treg cells in these patients, we could confirm decreased HPGD levels in Treg cells in two independent T2D cohorts. This supports the murine data that Treg-cell-derived 15-keto PGE_2 was important for maintenance of adipose tissue homeostasis. Although we do not have direct evidence to support the claim that lower expression of HPGD in Treg cells is causative for the development of T2D in humans, our data support a clear association between lower HPGD levels in Treg cells and decreased Treg cell functionality in T2D.

Altogether, with the Treg-cell-specific expression of HPGD, we have presented an enzymatic mechanism of Treg-cell-mediated suppression that is most likely tissue and context dependent, due to spatiotemporally regulated production of PGE_2 with high relevance for the maintenance of visceral adipose tissue homeostasis.

STAR★METHODS

Detailed methods are provided in the online version of this paper and include the following:

SUPPLEMENTAL INFORMATION

Supplemental Information can be found online at https://doi.org/10.1016/j.immuni.2019.03.014.

ACKNOWLEDGMENTS

We thank M. Schell, H. Theis, and M. Kraut for technical assistance; J. Oldenburg for blood samples from healthy individuals; B. Balderas and N. Warner for providing HPGD antibody; C. Benoist for microarray and clinical data from T2D patients; A. Rudensky for Foxp3-Cre-YFP mice; and W. Kastenmüller for critical discussions. CD1d tetramer and unloaded control tetramer were kindly provided by the NIH tetramer core facility. M. Beyer was funded by the Wilhelm-Sander-Foundation and the German Research Foundation (GRF) (SFB 832 and BE 4427/3-1). J.L.S. was funded by the GRF (SFB 832, SFB 704, INST 217/576-1, and INST 217/577-1). I.F. was funded by the GRF (SFB 704). M. Beyer, J.L.S., W.K., and I.F. are members of the excellence cluster

ImmunoSensation2 (EXC2151-390873048). N.F. is supported by the LOEWE program from the state of Hesse (Translational Medicine and Pharmacology). S.C.B. is supported by NHMRC project grants 339123 and 565314. K.S. and A.J.D. received support from the Breast Cancer Research Foundation.

AUTHOR CONTRIBUTIONS

L.S., Y.T., and E.S. performed qPCR, WB, overexpression experiments and functional analysis, murine experiments, and analyzed data; W.K. performed histone methylation studies; K.K., K.B., K.H., T.U., and J.S. performed bioinformatic analysis; M.S. and S.V.S. performed HPGD overexpression; Z.A., D.S., M.K., A.-K.B., A.E.P., C.O.-S., S.N., O.S., I.F., and H.W. performed and analyzed *in vivo* experiments; S.B. and T.V. performed *in vitro* assays; K.S. and A.J.D. analyzed HPGD activity; A.W. performed, designed, and supervised DNA methylation experiments; N.F. supervised the LC-MS/MS experiments; N.O., T.S., M. Blüher, S.S., and L.J.M. provided vital analytical tools; C.W. performed IHC; T.S. and S.C.B. designed, performed, and supervised ChIP experiments; F.C., A.P., and F.T.W. designed and performed metabolic experiments; and J.L.S. and M. Beyer supervised and analyzed experiments and wrote the manuscript. All authors discussed the results and commented on the manuscript.

DECLARATION OF INTERESTS

J.L.S. and M. Beyer have applied for several US and international patents on T_{reg} cell biology.

Received: April 4, 2018
Revised: December 20, 2018
Accepted: March 15, 2019
Published: April 23, 2019

REFERENCES

Bapat, S.P., Myoung Suh, J., Fang, S., Liu, S., Zhang, Y., Cheng, A., Zhou, C., Liang, Y., LeBlanc, M., Liddle, C., et al. (2015). Depletion of fat-resident Treg cells prevents age-associated insulin resistance. Nature *528*, 137–141.

Bernstein, B.E., Stamatoyannopoulos, J.A., Costello, J.F., Ren, B., Milosavljevic, A., Meissner, A., Kellis, M., Marra, M.A., Beaudet, A.L., Ecker, J.R., et al. (2010). The NIH Roadmap Epigenomics Mapping Consortium. Nat. Biotechnol. *28*, 1045–1048.

Beyer, M., Abdullah, Z., Chemnitz, J.M., Maisel, D., Sander, J., Lehmann, C., Thabet, Y., Shinde, P.V., Schmidleithner, L., Köhne, M., et al. (2016). Tumor-necrosis factor impairs CD4(+) T cell-mediated immunological control in chronic viral infection. Nat. Immunol. *17*, 593–603.

Beyer, M., Thabet, Y., Müller, R.U., Sadlon, T., Classen, S., Lahl, K., Basu, S., Zhou, X., Bailey-Bucktrout, S.L., Krebs, W., et al. (2011). Repression of the genome organizer SATB1 in regulatory T cells is required for suppressive function and inhibition of effector differentiation. Nat. Immunol. *12*, 898–907.

Boniface, K., Bak-Jensen, K.S., Li, Y., Blumenschein, W.M., McGeachy, M.J., McClanahan, T.K., McKenzie, B.S., Kastelein, R.A., Cua, D.J., and de Waal Malefyt, R. (2009). Prostaglandin E2 regulates Th17 cell differentiation and function through cyclic AMP and EP2/EP4 receptor signaling. J. Exp. Med. *206*, 535–548.

Burzyn, D., Kuswanto, W., Kolodin, D., Shadrach, J.L., Cerletti, M., Jang, Y., Sefik, E., Tan, T.G., Wagers, A.J., Benoist, C., and Mathis, D. (2013). A special population of regulatory T cells potentiates muscle repair. Cell *155*, 1282–1295.

Chemnitz, J.M., Driesen, J., Classen, S., Riley, J.L., Debey, S., Beyer, M., Popov, A., Zander, T., and Schultze, J.L. (2006). Prostaglandin E2 impairs CD4+ T cell activation by inhibition of lck: implications in Hodgkin's lymphoma. Cancer Res. *66*, 1114–1122.

Cipolletta, D., Cohen, P., Spiegelman, B.M., Benoist, C., and Mathis, D. (2015). Appearance and disappearance of the mRNA signature characteristic of Treg cells in visceral adipose tissue: age, diet, and PPARγ effects. Proc. Natl. Acad. Sci. USA *112*, 482–487.

Cipolletta, D., Feuerer, M., Li, A., Kamei, N., Lee, J., Shoelson, S.E., Benoist, C., and Mathis, D. (2012). PPAR-γ is a major driver of the accumulation and phenotype of adipose tissue Treg cells. Nature *486*, 549–553.

Coggins, K.G., Latour, A., Nguyen, M.S., Audoly, L., Coffman, T.M., and Koller, B.H. (2002). Metabolism of PGE2 by prostaglandin dehydrogenase is essential for remodeling the ductus arteriosus. Nat. Med. *8*, 91–92.

Deng, T., Liu, J., Deng, Y., Minze, L., Xiao, X., Wright, V., Yu, R., Li, X.C., Blaszczak, A., Bergin, S., et al. (2017). Adipocyte adaptive immunity mediates diet-induced adipose inflammation and insulin resistance by decreasing adipose Treg cells. Nat. Commun. *8*, 15725.

Eruslanov, E., Kaliberov, S., Daurkin, I., Kaliberova, L., Buchsbaum, D., Vieweg, J., and Kusmartsev, S. (2009). Altered expression of 15-hydroxyprostaglandin dehydrogenase in tumor-infiltrated CD11b myeloid cells: a mechanism for immune evasion in cancer. J. Immunol. *182*, 7548–7557.

Ferraro, A., D'Alise, A.M., Raj, T., Asinovski, N., Phillips, R., Ergun, A., Replogle, J.M., Bernier, A., Laffel, L., Stranger, B.E., et al. (2014). Interindividual variation in human T regulatory cells. Proc. Natl. Acad. Sci. USA *111*, E1111–E1120.

Feuerer, M., Herrero, L., Cipolletta, D., Naaz, A., Wong, J., Nayer, A., Lee, J., Goldfine, A.B., Benoist, C., Shoelson, S., and Mathis, D. (2009). Lean, but not obese, fat is enriched for a unique population of regulatory T cells that affect metabolic parameters. Nat. Med. *15*, 930–939.

Harmon, G.S., Dumlao, D.S., Ng, D.T., Barrett, K.E., Dennis, E.A., Dong, H., and Glass, C.K. (2010). Pharmacological correction of a defect in PPAR-gamma signaling ameliorates disease severity in Cftr-deficient mice. Nat. Med. *16*, 313–318.

He, W., Barak, Y., Hevener, A., Olson, P., Liao, D., Le, J., Nelson, M., Ong, E., Olefsky, J.M., and Evans, R.M. (2003). Adipose-specific peroxisome proliferator-activated receptor gamma knockout causes insulin resistance in fat and liver but not in muscle. Proc. of the Natl. Acad. Sci. USA *100*, 15712–15717.

Hill, J.A., Feuerer, M., Tash, K., Haxhinasto, S., Perez, J., Melamed, R., Mathis, D., and Benoist, C. (2007). Foxp3 transcription-factor-dependent and -independent regulation of the regulatory T cell transcriptional signature. Immunity *27*, 786–800.

Huynh, A., DuPage, M., Priyadharshini, B., Sage, P.T., Quiros, J., Borges, C.M., Townamchai, N., Gerriets, V.A., Rathmell, J.C., Sharpe, A.H., et al. (2015). Control of PI(3) kinase in Treg cells maintains homeostasis and lineage stability. Nat. Immunol. *16*, 188–196.

Josefowicz, S.Z., Lu, L.F., and Rudensky, A.Y. (2012). Regulatory T cells: mechanisms of differentiation and function. Annu. Rev. Immunol. *30*, 531–564.

Kaizer, E.C., Glaser, C.L., Chaussabel, D., Banchereau, J., Pascual, V., and White, P.C. (2007). Gene expression in peripheral blood mononuclear cells from children with diabetes. J. Clin. Endocrinol. Metab. *92*, 3705–3711.

Kalinski, P. (2012). Regulation of immune responses by prostaglandin E2. J. Immunol. *188*, 21–28.

Klotz, L., Burgdorf, S., Dani, I., Saijo, K., Flossdorf, J., Hucke, S., Alferink, J., Nowak, N., Beyer, M., Mayer, G., et al. (2009). The nuclear receptor PPAR gamma selectively inhibits Th17 differentiation in a T cell-intrinsic fashion and suppresses CNS autoimmunity. J. Exp. Med. *206*, 2079–2089.

Kolodin, D., van Panhuys, N., Li, C., Magnuson, A.M., Cipolletta, D., Miller, C.M., Wagers, A., Germain, R.N., Benoist, C., and Mathis, D. (2015). Antigen- and cytokine-driven accumulation of regulatory T cells in visceral adipose tissue of lean mice. Cell Metab. *21*, 543–557.

Lee, P.P., Fitzpatrick, D.R., Beard, C., Jessup, H.K., Lehar, S., Makar, K.W., Pérez-Melgosa, M., Sweetser, M.T., Schlissel, M.S., Nguyen, S., et al. (2001). A critical role for Dnmt1 and DNA methylation in T cell development, function, and survival. Immunity *15*, 763–774.

Li, C., DiSpirito, J.R., Zemmour, D., Spallanzani, R.G., Kuswanto, W., Benoist, C., and Mathis, D. (2018). TCR transgenic mice reveal stepwise, multi-site acquisition of the distinctive fat-Treg phenotype. Cell *174*, 285–299.e12.

Lumeng, C.N., Bodzin, J.L., and Saltiel, A.R. (2007). Obesity induces a phenotypic switch in adipose tissue macrophage polarization. J. Clin. Invest. *117*, 175–184.

Maddox, J.F., and Serhan, C.N. (1996). Lipoxin A4 and B4 are potent stimuli for human monocyte migration and adhesion: selective inactivation by dehydrogenation and reduction. J. Exp. Med. *183*, 137–146.

Malek, T.R., Yu, A., Vincek, V., Scibelli, P., and Kong, L. (2002). CD4 regulatory T cells prevent lethal autoimmunity in IL-2Rbeta-deficient mice. Implications for the nonredundant function of IL-2. Immunity *17*, 167–178.

Myung, S.J., Rerko, R.M., Yan, M., Platzer, P., Guda, K., Dotson, A., Lawrence, E., Dannenberg, A.J., Lovgren, A.K., Luo, G., et al. (2006). 15-Hydroxyprostaglandin dehydrogenase is an in vivo suppressor of colon tumorigenesis. Proc. Natl. Acad. Sci. USA *103*, 12098–12102.

Newman, A.M., Liu, C.L., Green, M.R., Gentles, A.J., Feng, W., Xu, Y., Hoang, C.D., Diehn, M., and Alizadeh, A.A. (2015). Robust enumeration of cell subsets from tissue expression profiles. Nat. Methods *12*, 453–457.

Picelli, S., Björklund, Å.K., Faridani, O.R., Sagasser, S., Winberg, G., and Sandberg, R. (2013). Smart-seq2 for sensitive full-length transcriptome profiling in single cells. Nat. Methods *10*, 1096–1098.

Roizen, J.D., Asada, M., Tong, M., Tai, H.H., and Muglia, L.J. (2008). Preterm birth without progesterone withdrawal in 15-hydroxyprostaglandin dehydrogenase hypomorphic mice. Mol. Endocrinol. *22*, 105–112.

Rubtsov, Y.P., Rasmussen, J.P., Chi, E.Y., Fontenot, J., Castelli, L., Ye, X., Treuting, P., Siewe, L., Roers, A., Henderson, W.R., Jr., et al. (2008). Regulatory T cell-derived interleukin-10 limits inflammation at environmental interfaces. Immunity *28*, 546–558.

Sadlon, T.J., Wilkinson, B.G., Pederson, S., Brown, C.Y., Bresatz, S., Gargett, T., Melville, E.L., Peng, K., D'Andrea, R.J., Glonek, G.G., et al. (2010). Genome-wide identification of human FOXP3 target genes in natural regulatory T cells. J. Immunol. *185*, 1071–1081.

Schmitz, K., de Bruin, N., Bishay, P., Männich, J., Häussler, A., Altmann, C., Ferreirós, N., Lötsch, J., Ultsch, A., Parnham, M.J., et al. (2014). R-flurbiprofen attenuates experimental autoimmune encephalomyelitis in mice. EMBO Mol. Med. *6*, 1398–1422.

Sharma, S., Yang, S.C., Zhu, L., Reckamp, K., Gardner, B., Baratelli, F., Huang, M., Batra, R.K., and Dubinett, S.M. (2005). Tumor cyclooxygenase-2/prostaglandin E2-dependent promotion of FOXP3 expression and CD4+ CD25+ T regulatory cell activities in lung cancer. Cancer Res. *65*, 5211–5220.

Shinkai, Y., Rathbun, G., Lam, K.-P., Oltz, E.M., Stewart, V., Mendelsohn, M., Charron, J., Datta, M., Young, F., Stall, A.M., and Alt, F.W. (1992). RAG-2-deficient mice lack mature lymphocytes owing to inability to initiate V(D)J rearrangement. Cell *68*, 855–867.

Shrestha, S., Yang, K., Guy, C., Vogel, P., Neale, G., and Chi, H. (2015). Treg cells require the phosphatase PTEN to restrain TH1 and TFH cell responses. Nat. Immunol. *16*, 178–187.

Subbaramaiah, K., Howe, L.R., Zhou, X.K., Yang, P., Hudis, C.A., Kopelovich, L., and Dannenberg, A.J. (2012). Pioglitazone, a PPARγ agonist, suppresses CYP19 transcription: evidence for involvement of 15-hydroxyprostaglandin dehydrogenase and BRCA1. Cancer Prev. Res. (Phila.) *5*, 1183–1194.

Tai, H.H., Cho, H., Tong, M., and Ding, Y. (2006). NAD+-linked 15-hydroxyprostaglandin dehydrogenase: structure and biological functions. Curr. Pharm. Des. *12*, 955–962.

Tangen, S.E., Tsinajinnie, D., Nunez, M., Shaibi, G.Q., Mandarino, L.J., and Coletta, D.K. (2013). Whole blood gene expression profiles in insulin resistant Latinos with the metabolic syndrome. PloS One *8*, e84002.

ten Hove, T., van den Blink, B., Pronk, I., Drillenburg, P., Peppelenbosch, M.P., and van Deventer, S.J.H. (2002). Dichotomal role of inhibition of p38 MAPK with SB 203580 in experimental colitis. Gut *50*, 507–512.

Uppal, S., Diggle, C.P., Carr, I.M., Fishwick, C.W., Ahmed, M., Ibrahim, G.H., Helliwell, P.S., Latos-Bieleńska, A., Phillips, S.E., Markham, A.F., et al. (2008). Mutations in 15-hydroxyprostaglandin dehydrogenase cause primary hypertrophic osteoarthropathy. Nat. Genet. *40*, 789–793.

van der Maaten, L., and Hinton, G. (2008). Visualizing data using t-SNE. J. Mach. Learn. Res. *9*, 2579–2605.

Vasanthakumar, A., Moro, K., Xin, A., Liao, Y., Gloury, R., Kawamoto, S., Fagarasan, S., Mielke, L.A., Afshar-Sterle, S., Masters, S.L., et al. (2015). The transcriptional regulators IRF4, BATF and IL-33 orchestrate development and maintenance of adipose tissue-resident regulatory T cells. Nat. Immunol. *16*, 276–285.

Vignali, D. (2008). How many mechanisms do regulatory T cells need? Eur. J. Immunol. *38*, 908–911.

Wagner, E.J., and Carpenter, P.B. (2012). Understanding the language of Lys36 methylation at histone H3. Nat. Rev. Mol. Cell Biol. *13*, 115–126.

Wan, Y.Y., and Flavell, R.A. (2005). Identifying Foxp3-expressing suppressor T cells with a bicistronic reporter. Proc. Natl. Acad. Sci. USA *102*, 5126–5131.

Wensveen, F.M., Jelenčić, V., Valentić, S., Šestan, M., Wensveen, T.T., Theurich, S., Glasner, A., Mendrila, D., Štimac, D., Wunderlich, F.T., et al. (2015). NK cells link obesity-induced adipose stress to inflammation and insulin resistance. Nat. Immunol. *16*, 376–385.

Yao, C., Sakata, D., Esaki, Y., Li, Y., Matsuoka, T., Kuroiwa, K., Sugimoto, Y., and Narumiya, S. (2009). Prostaglandin E2-EP4 signaling promotes immune inflammation through Th1 cell differentiation and Th17 cell expansion. Nat. Med. *15*, 633–640.

Zhang, Y., Desai, A., Yang, S.Y., Bae, K.B., Antczak, M.I., Fink, S.P., Tiwari, S., Willis, J.E., Williams, N.S., Dawson, D.M., et al. (2015). TISSUE REGENERATION. Inhibition of the prostaglandin-degrading enzyme 15-PGDH potentiates tissue regeneration. Science *348*, aaa2340.

STAR★METHODS

KEY RESOURCES TABLE

REAGENT or RESOURCE	SOURCE	IDENTIFIER
Antibodies		
Ultra-LEAF purified anti-mouse CD16/32 Antibody, Clone 93	BioLegend	Cat# 101330, RRID: AB_2561482
APC-Cyanine7 anti-mouse/human CD45R/B220 Antibody, Clone RA3-6B2	BioLegend	Cat# 103224, RRID: AB_313007
Brilliant Violet 605 anti-mouse/human CD11b Antibody, Clone M1/70	BioLegend	Cat# 101237, RRID: AB_11126744
PE anti-mouse CD11c Antibody, Clone N418	BioLegend	Cat# 117307, RRID: AB_313776
Brilliant Violet 421 anti-mouse CD127 (IL-7R) Antibody, Clone A7R34	BioLegend	Cat# 135024, RRID: AB_11218800
Alexa Fluor 647 anti-mouse CD19 Antibody, Clone eBio1D3	eBioscience	Cat# 51-0193-80, RRID: AB_657654
PE-Cyanine7 anti-mouse CD25 Antibody, Clone PC61	BioLegend	Cat# 102016, RRID: AB_312865
Brilliant Violet 510 anti-mouse CD25 Antibody, Clone PC61	BioLegend	Cat# 102042, RRID: AB_2562270
FITC anti-mouse CD3 Antibody, Clone 17A2	BioLegend	Cat# 100203, RRID: AB_312660
PE/Dazzle 594 anti-mouse CD3 Antibody, Clone 17A2	BioLegend	Cat# 100246, RRID: AB_2565883
Brilliant Violet 605 anti-mouse CD3 Antibody, Clone 17A2	BioLegend	Cat# 100237, RRID: AB_2562039
PerCP/Cy5.5 anti-mouse CD4 Antibody, Clone RM4-5	BioLegend	Cat# 100540, RRID: AB_893326
Brilliant Violet 650 anti-mouse CD4 Antibody, Clone RM4-5	BioLegend	Cat# 100555, RRID: AB_2562529
Pacific Blue anti-mouse/human CD44 Antibody, Clone IM7	BioLegend	Cat# 103020, RRID: AB_493683
Alexa Fluor 488 anti-mouse CD45 Antibody, Clone 30-F11	BioLegend	Cat# 103122, RRID: AB_493531
PerCP/Cy5.5 anti-mouse CD45 Antibody, Clone 30-F11	BioLegend	Cat# 103132, RRID: AB_893340
Alexa Fluor 647 anti-mouse CD62L Antibody, Clone MEL-14	BioLegend	Cat# 104421, RRID: AB_493379
APC anti-mouse CD69 Antibody, Clone H1.2F3	eBioscience	Cat# 17-0691-80, RRID: AB_1210796
PE anti-mouse CD152 (CTLA-4) Antibody, Clone UC10-4B9	eBioscience	Cat# 12-1522-83, RRID: AB_465880
eFluor 660 anti-mouse Eos Antibody, Clone ESB7C2	eBioscience	Cat# 50-5758-80, RRID: AB_2574242
PerCP/Cy5.5 anti-mouse F4/80 Antibody, Clone BM8	BioLegend	Cat# 123128, RRID: AB_893484
PE-eFluor 610 anti-mouse FOXP3 Antibody, Clone FJK-16 s	eBioscience	Cat# 61-5773-80, RRID: AB_2574623
eFluor 450 anti-mouse FOXP3 Antibody, Clone FJK-16 s	eBioscience	Cat# 48-5773-82, RRID: AB_1518812
Alexa Fluor 488 anti-mouse FOXP3 Antibody, Clone FJK-16 s	eBioscience	Cat# 53-5773-80, RRID: AB_469916

(*Continued on next page*)

Continued

REAGENT or RESOURCE	SOURCE	IDENTIFIER
Alexa Fluor 488 GFP Tag polyclonal Antibody	Invitrogen	Cat# A-21311, RRID: AB_221477
PE anti-mouse CD357 (GITR) Antibody, Clone DTA-1	BioLegend	Cat# 126310, RRID: AB_1089130
PerCP/Cy5.5 anti-mouse Ly-6G/Ly-6C (Gr-1) Antibody, Clone RB6-8C5	BioLegend	Cat# 108427, RRID: AB_893561
eFluor 450 anti-mouse HELIOS Antibody, Clone 22F6	eBioscience	Cat# 48-9883-41, RRID: AB_2574137
PerCP/eFluor 710 anti-mouse CD278 (ICOS) Antibody, Clone 15F9	eBioscience	Cat# 46-9940-80, RRID: AB_11041534
PE-Cyanine7 anti-mouse IFN-gamma Antibody, Clone XMG1.2	eBioscience	Cat# 25-7311-82, RRID: AB_469680
APC anti-mouse IL-17A Antibody, Clone eBio17B7	eBioscience	Cat# 17-7177-81, RRID: AB_763580
Brilliant Violet 421 anti-mouse IL-4 Antibody, Clone 11B11	BioLegend	Cat# 504127, RRID: AB_2562594
eFluor 660 anti-mouse Ki-67 Antibody, Clone SolA15	eBioscience	Cat# 50-5698-82, RRID:AB_2574235
PerCP/eFluor 710 anti-mouse Ki-67 Antibody, Clone SolA15	eBioscience	Cat# 46-5698-80, RRID: AB_11039489
PE-Cyanine7 anti-mouse KLRG1 Antibody, Clone 2F1	eBioscience	Cat# 25-5893-80, RRID: AB_1518769
Brilliant Violet 510 anti-mouse Ly-6C antibody, Clone HK1.4	BioLegend	Cat# 128033, RRID: AB_2562351
APC anti-mouse Ly-6G (Gr-1) Antibody, Clone 1A8-Ly6g	eBioscience	Cat# 17-9668-82, RRID: AB_2573307
PE-Cyanine7 anti-mouse CD304 (Neuropilin-1) Antibody, Clone 3E12	BioLegend	Cat# 145211, RRID: AB_2562359
Brilliant Violet 421 anti-mouse NK-1.1 Antibody, Clone PK136	BioLegend	at# 108732, RRID: AB_2562218
Brilliant Violet 510 anti-mouse CD335 (NKp46) Antibody, Clone 29A1.4	BioLegend	Cat# 137623, RRID: AB_2563290
PerCP/Cy5.5 anti-mouse IL-33R (IL1RL1, ST2) Antibody, Clone DIH9	BioLegend	Cat# 145312, RRID: AB_2565636
Alexa Fluor 647 anti-mouse CD206 (MMR) Antibody, Clone C068C2	BioLegend	Cat# 141711, RRID: AB_10900240
Brilliant Violet 421 anti-mouse I-A/I-E Antibody, Clone M5/114.15.2	BioLegend	Cat# 107631, RRID: AB_10900075
PE-Cyanine7 anti-mouse CD14 Antibody, Clone Sa14-2	BioLegend	Cat# 123316, RRID: AB_10645329
Unconjugated anti-human CD3 Antibody, Clone OKT3	Ortho Biotech	Cat# OKT3, RRID: AB_2619696
Unconjugated anti-human CD28, Clone 9.3	Kind gift from J.L. Riley	RRID: AB_2687729
Unconjugated anti-human MHC I Antibody, Clone W6/32	Thermo Fisher Scientific	Cat# MA1-22572, RRID: AB_560084
Unconjugated mouse anti-human IgG pure monoclonal Antibody, Clone IS11-3B2.2.3	Miltenyi Biotec	Cat# 130-093-197, RRID: AB_1036180
PerCP/Cy5.5 anti-human CD127 (IL-7R) Antibody, Clone A019D5	BioLegend	Cat# 351321, RRID: AB_10900253
PE-Cyanine7 anti-human CD25 Antibody, Clone BC96	BioLegend	Cat# 302612, RRID: AB_314282
Brilliant Violet 421 anti-human CD3 Antibody, Clone UCHT1	BioLegend	Cat# 300434, RRID: AB_10962690

(*Continued on next page*)

Continued

REAGENT or RESOURCE	SOURCE	IDENTIFIER
APC anti-human CD4 Antibody, Clone RPA-T4	BioLegend	Cat# 300514, RRID: AB_314082
PE anti-human FOXP3 Antibody, Clone PCH101	eBioscience	Cat# 12-4776-42, RRID: AB_1518782
FITC anti-human CD45RA Antibody, Clone HI100	BD Biosciences	Cat# 555488, RRID: AB_395879
PE anti-human CD45RO Antibody, Clone UCHL1	BD Biosciences	Cat# 347967, RRID: AB_400362
Pacific Blue anti-human CD14 Antibody, Clone HCD14	BioLegend	Cat# 325616, RRID: AB_830689
PE-Cyanine7 anti-human CD86 (B7-2) Antibody, Clone IT2.2	eBioscience	Cat# 25-0869-42, RRID: AB_2573374
Unconjugated anti-mouse F4/80 Antibody, Clone CI:A3-1	Abcam	Cat# ab6640, RRID: AB_1140040
Biotin conjugated rabbit anti-rat IgG (H+L) secondary Antibody,	Thermo Fisher Scientific	Cat# 31834, RRID: AB_228448
Unconjugated anti-mouse Phospho-Akt (Ser473) Antibody	Cell Signaling Technology	Cat# 9271, RRID: AB_329825
Unconjugated anti-mouse Akt (pan) (40D4) polyclonal Antibody	Cell Signaling Technology	Cat# 2920, RRID: AB_1147620
Unconjugated anti-human HPGD Antibody, Clone C3A7	kind gift of Robert Balderas	N/A
Unconjugated anti-mouse/human Actin Antibody, clone C4 antibody	Millipore	Cat# MAB1501, RRID: AB_2223041
Unconjugated anti-mouse/human FABP4 antibody	Cell Signaling Technology	Cat# 2120, RRID: AB_2102466
Unconjugated anti-mouse/human Calnexin C-Terminal (575-593) polyclonal antibody	Millipore	Cat# 208880, RRID: AB_2069031
HRP conjugated anti-rabbit IgG Antibody	GE Healthcare	Cat# GENA934, RRID: AB_2722659
HRP conjugated anti-mouse IgG Antibody	GE Healthcare	Cat# NA9310-1ml, RRID: AB_772193
Unconjugated anti-mouse/human/rat Stat5 polyclonal Antibody	Santa Cruz	Cat# sc-835-G, RRID: AB_632447
Unconjugated rabbit anti-mouse IgG H&L polyclonal Antibody	Abcam	Cat# ab6709, RRID: AB_956006
Unconjugated rabbit anti-mouse IgG H&L polyclonal Antibody	Abcam	Cat# ab46540, RRID: AB_2614925
Unconjugated anti-mouse/human FOXP3 Antibody	Novus	Cat# NB600-245, RRID: AB_10001076
Unconjugated rabbit anti-human Acetyl-Histone H4 polyclonal Antibody – ChIP Grade	Millipore	Cat# 17-630, RRID: AB_11210569
Unconjugated rabbit anti-human Trimethyl-Histone H3 (Lys4) polyclonal Antibody – ChIP Grade	Millipore	Cat# 17-614, RRID: AB_11212770
Unconjugated rabbit anti-human Histone H3, trimethyl (Lys27) polyclonal Antibody – ChIP Grade	Millipore	Cat# 17-622, RRID: AB_916347
Unconjugated rabbit normal IgG Control Antibody – ChIP Grade	Millipore	Cat# 12-370, RRID: AB_145841
Unconjugated 6X His tag polyclonal Antibody – ChIP Grade	Abcam	Cat# ab9108, RRID: AB_307016
Bacterial and Virus Strains		
E.coli K12, strain DH5α	DSMZ	DSM# 6897
E.coli, strain Stbl3	Thermo Fisher Scientific	Cat# C737303

(*Continued on next page*)

Continued

REAGENT or RESOURCE	SOURCE	IDENTIFIER
Biological Samples		
Buffy-coat samples	Universityhospital, Bonn	Reg. No. 288/13
T2D/Healthy patient whole blood samples	Universityhospital, Leipzig	Reg. No. 017-12-23012012
pGL4.24[luc2P/minP] Vector	Promega	Cat# E8411
pRRLSIN.cPPT.PGK-GFP.WPRE Vector (hPGK)	Addgene	Plasmid #12252
Chemicals, Peptides, and Recombinant Proteins		
Collagenase I	Sigma Aldrich	Cat# C6885
DNase I	Sigma Aldrich	Cat# 11284932001
Collagenase IV	Sigma Aldrich	Cat# C5138
Liberase	Sigma Aldrich	Cat# 05401127001
RNase inhibitor	Takara Clontech	Cat# 2313B
Superscript II Reverse Transcriptase	Thermo Fisher Scientific	Cat# 18064014
KAPA HiFi HotStart ReadyMix	Kapa Biosystems	Cat# KR0370
High Sensitivity D5000 ScreenTape	Agilent Technologies	Cat# 5067-5592
High Sensitivity D5000 Reagents & Ladder	Agilent Technologies	Cat# 5067-5593
Recombinant human TGF-β1 (HEK293 derived)	PeproTech	Cat# 100-21
IL-2 (Proleukin)	Chiron/Novartis	PZN# 2238131
rmIL-12	PeproTech	Cat# 210-12
rhIL-4	Immunotools	Cat# 11340048
rhGM-CSF	Immunotools	Cat# 11343128
rmM-CSF	Immunotools	Cat# 12343118
rmGM-CSF	Immunotools	Cat# 12343128
rmIL-4	Immunotools	Cat# 12340045
rmIL-21	PeproTech	Cat# 11343161
rmIL-33	BioLegend	Cat# 580502
Unconjugated anti-mouse CD3 Antibody, Clone 17A2	BioLegend	Cat# 100201
Unconjugated anti-mouse CD28 Antibody, Clone 37.51	BioLegend	Cat# 102101
PGE_2	Cayman Chemicals	Cat# 14010 CAS 363-24-6
15-keto-PGE_2	Cayman Chemicals	Cat# 14720 CAS 26441-05-4
PGF_{2a}	Cayman Chemicals	Cat# 16010 CAS 551-11-1
PGD_2	Cayman Chemicals	Cat# 12010 CAS 41598-07-6
PGJ_2	Cayman Chemicals	Cat# 18500 CAS 60203-57-8
Janex-1	Cayman Chemicals	Cat# 10011246-5
STAT5 Inhibitor	Merck	Cat# 573108 CAS 285986-31-4
PD98059	Merck	Cat# 19-143
Pioglitazone	Cayman Chemicals	Cat# 71745 CAS 111025-46-8
Rosiglitazone	Cayman Chemicals	Cat# 71740 CAS 122320-73-4
cOmplete Protease Inhibitor Cocktail	Roche	Cat# 04693116001
PhosSTOP	Roche	Cat# PHOSS-RO
Xho I	NEB	Cat# R0146
BglII	NEB	Cat# R0144
Nhe I	NEB	Cat# R0131
Hind III	NEB	Cat# R0104
SuperScript III One-Step RT-PCR System with Platinum Taq High Fidelity DNA Polymerase	Thermo Fisher Scientific	Cat# 12574030

(*Continued on next page*)

Continued

REAGENT or RESOURCE	SOURCE	IDENTIFIER
Dynabeads Mouse T-Activator CD3/CD28 for T Cell Expansion and Activation	Thermo Fisher Scientific	Cat# 11456D
MyTaq HS DNA Polymerase	Boline	Cat# BIO-21111
Cell Stimulation Cocktail (500X)	eBioscience	Cat# 00-4970-03
DirectPCR Lysis Reagent Tail	Peqlab	Cat# 31-101-T
CFSE	eBioscience	Cat# 65-0850-84
Cell Proliferation Dye eFluor 670	eBioscience	Cat# 65-0840-85
Critical Commercial Assays		
Foxp3 / Transcription Factor Staining Buffer Set	eBioscience	Cat# 00-5523-00
CD4 M-pluriBead anti-human M-kit	Pluriselect	Cat# 19-00400-20 and 70-50010-21
RosetteSep Human CD4+ T Cell Enrichment Cocktail	Stem Cell	Cat# 15022
CD25 MicroBeads II, human	Miltenyi Biotec	Cat# 130-092-983
CD45RA MicroBeads, human	Miltenyi Biotec	Cat# 130-045-901
Universal ProbeLibrary Set, Human	Roche	Cat# 4683633001
Transcriptor First Strand cDNA synthesis kit	Roche	Cat# 4897030001
Maxima SYBR Green Master	Thermo Fisher Scientific	Cat# K0221
LightCycler 480 Probes Master	Roche	Cat# 4887301001
Dual-Luciferase Reporter Assay System	Promega	Cat# E1910
Prostaglandin E Metabolite ELISA Kit	Cayman Chemicals	Cat# 514531
miRNeasy Mini Kit	QIAGEN	Cat# 217004
TruSeq RNA Library Prep Kit v2	Illumina	Cat# RS-122-2001
TruSeq ChIP Library Preparation Kit	Illumina	Cat# IP-202-1012
Multiplexing Sample Preparation Oligonucleotide Kit	Illumina	Cat# PE-400-1001
Nextera XT DNA Library Preparation Kit	Illumina	Cat# FC-131-1024
QIAquick Gel Extraction Kit	QIAGEN	Cat# 28704
QIAquick PCR Purification Kit	QIAGEN	Cat# 28104
MagniSort Human CD19 Positive Selection Kit	eBioscience	Cat# 8802-6833-74
MojoSort Human NK Cell Isolation Kit	Biolegend	Cat# 480053
Ultrasensitive Mouse Insulin ELISA	Mercodia	Cat# 10-1249-01
Human T Cell Nucleofector Kit	Lonza	Cat# VPA-1002
LIVE/DEAD Fixable Near-IR Dead Cell Stain Kit	Thermo Fisher Scientific	Cat# L10119
Deposited Data		
Tiling array Data	Sadlon et al., 2010	GEO: GSE20995
Microarray Data	Beyer et al., 2011	GEO: GSE15390
RNA-seq Data	This paper	GEO: GSE62579 and GSE123888
MeDIP-seq Data	http://trace.ddbj.nig.ac.jp	DRP000902
T2D Paxgene Data	Kaizer et al., 2007 and Tangen et al., 2013	GEO: GSE9006 and E-MTAB-1954
Histone Modification Dataset	GEO NIH Roadmap Epigenomics	http://www.roadmapepigenomics.org
Murine Immune Cell Dataset	http://www.immgen.org	GEO: GSE15907 and GSE37448
Murine Immune Cell Dataset	http://www.nextbio.com	N/A
T2D Treg-cell Dataset	Ferraro et al., 2014	N/A
VAT Treg-cell Signature	Feuerer et al., 2009	GEO: GSE7852

(*Continued on next page*)

Continued		
REAGENT or RESOURCE	SOURCE	IDENTIFIER
PPAR-γ as determinant for VAT Treg-cell gene expression Dataset	Cipolletta et al., 2012; Cipolletta et al., 2015 and Li et al., 2018	GEO: GSE37535 and GSE113393
Murine Treg-cell Signature	Hill et al., 2007	GEO: GSE7460
Experimental Models: Cell Lines		
HEK293T	ATCC	Cat# CRL-3216, RRID: CVCL_0063
Jurkat	DSMZ	DSMZ Cat# ACC-282, RRID: CVCL_0065
3T3-L1	ATCC	Cat# CCL-92.1, RRID: CVCL_0123
Experimental Models: Organisms/Strains		
Foxp3$^{YFP\text{-}Cre}$	JAX	Published in Rubtsov et al., 2008
Hpgd$^{fl/fl}$	Laboratory of Prof. Louis J. Muglia, Cincinnati's Children Hospital	Published in Roizen et al., 2008
Cd4^{Cre}	JAX	Published in Lee et al., 2001
Pparγ$^{fl/fl}$	JAX	Published in He et al., 2003
Foxp3$^{IRES\text{-}RFP}$	JAX	Published in Wan and Flavell, 2005
Rag2$^{-/-}$	JAX	Published in Shinkai et al., 1992
Oligonucleotides		
For oligonucleotide sequences, see Table S7	This paper	N/A
Software and Algorithms		
FlowJo	BD Biosciences	RRID: SCR_008520
LightCycler Software	Roche	RRID: SCR_012155
TopHat v2.0.11	http://tophat.cbcb.umd.edu/	RRID: SCR_013035
Partek Genomics Suite (PGS)	Partek Inc	RRID: SCR_011860
Kallisto v0.44 s	https://pachterlab.github.io/kallisto/about	RRID: SCR_016582
CellProfiler Image Analysis Software 2.0	http://cellprofiler.org	RRID: SCR_007358
Cytoscape	http://cytoscape.org	RRID: SCR_003032
BiNGO: A Biological Networks Gene Ontology tool	http://www.psb.ugent.be/cbd/papers/BiNGO/Home.html	RRID: SCR_005736
Graph Pad Prism	GraphPad Software	RRID: SCR_002798
Fiji ImageJ	http://fiji.sc	RRID: SCR_002285
Other		
mCD1d PBS-57 BV421	NIH	N/A
mCD1d unloaded BV421	NIH	N/A

CONTACT FOR REAGENT AND RESOURCE SHARING

Further information and requests for resources and reagents should be directed to and will be fulfilled by the Lead Contact, PD Dr. Marc Beyer (marc.beyer@dzne.de).

EXPERIMENTAL MODEL AND SUBJECT DETAILS

Human Subjects

Human T cells were purified from Buffy coats of healthy human donors obtained in compliance with institutional review board protocols (Ethics committee, University of Bonn, Reg. No. 288/13) after written consent. Due to privacy regulations, gender and age of these donors could not be ascertained. For analysis of T cells of T2D patients, blood was drawn from T2D patients and age matched healthy individuals after written informed consent after approval by the local ethics committee (Leipzig University, Reg. No. 017-12-23012012). Information on age and gender of these patients can be found in Table S6.

Mice

Foxp3$^{YFP\text{-}Cre}$, *Hpgd*$^{fl/fl}$, *Cd4*^{Cre}, *Ppar*$\gamma^{fl/fl}$, *Foxp3*$^{IRES\text{-}RFP}$ and *Rag2*$^{-/-}$ mice were previously described (Cipolletta et al., 2012; Klotz et al., 2009; Roizen et al., 2008; Rubtsov et al., 2008; Shinkai et al., 1992; Wan and Flavell, 2005). Mice were housed under specific pathogen-free conditions and used in accordance with the local legislation governing animal studies following The Principles of Laboratory Animal Care (NIH publication No. 85-23, revised in 1996). All animal experiments were approved by the Local Animal Care Commission of North Rhine-Westphalia (84-02.04.2013.A248, 87-51.04.2011.A019 and 84-02.04.2016.A282). In general, male animals between 6 and 10 weeks of age were used for experiments. In metabolic and phenotyping studies of older animals, 6-10 week old, 12-20 week old and > 40 week old animals were used.

Cell Lines

Human embryonic kidney (HEK) 293T (ATCC CRL-11268; female) and 3T3-L1 (ATCC CL-173; male) cells were maintained in DMEM containing 10% heat-inactivated fetal calf serum. Human Jurkat cells (DSMZ ACC-282) cells were maintained in RPMI containing 10% heat-inactivated fetal calf serum. Cells were cultivated at 37°C, 5%CO_2.

Microbe Strains

For genetic engineering, two different E.coli strains were used: DH5α (DSMZ) and Stbl3 (Thermo Fisher Scientific). Bacteria were cultivated in LB-medium containing plasmid-specific antibiotics.

METHOD DETAILS

Antibodies and Flow Cytometry Analysis

Flourescent-dye-conjugated antibodies were purchased from Becton Dickinson, BioLegend or eBioscience. Data were acquired on a BD LSRII or BD Symphony A5 flow cytometer (Becton Dickinson) and analyzed using FlowJo software package (FlowJo, LLC). Extracellular staining was performed at 4°C for 20 min. Intracellular staining of murine and human T cells was conducted using the Foxp3 Staining Buffer Kit (eBioscience) with the addition of FcR-blocking reagents (CD16/CD32 or human IgG). CD1d tetramers for staining were provided by the NIH Tetramer Core. Tetramer staining was performed in a 1:400 dilution for 15 min at RT.

Purification of Murine T Cells

Murine Cells were purified from thymus, spleen, peripheral and mesenteric lymph nodes, peripheral blood, bone marrow, lung, kidney, skin, colon, small intestine and brown and visceral adipose tissue by directly sorting on an BD Aria III cell sorter for CD3, CD4, CD25, and GFP$^+$ or YFP$^+$ cells respectively or following enrichment of CD4$^+$ T cells using the CD4 negative isolation kit (Miltenyi Biotech). Only cells isolated with a purity of > 98% were used for further analysis. Brown and visceral adipose tissue Treg and Tconv cells were isolated as previously described (Feuerer et al., 2009). Briefly, fat tissue was excised and minced after perfusing the animals. Subsequently, tissue was digested at 37°C for 40 min in DMEM containing 20 mg/ml BSA, 1 mg/ml Collagenase II (Sigma) and 20 μg/ml DNase I (Sigma Aldrich). The reaction was stopped by incubating with 4 μl/ml 0.5 M EDTA at RT for 2 min. To isolate tissue-resident Treg and Tconv cells, after perfusion, lungs and kidneys were digested for 45 min in RPMI containing 10 mM HEPES, 0.5 mg/ml Collagenase Type IV (Sigma Aldrich) and 0.05 mg/ml DNase I (Sigma Aldrich) at 37°C. Cells were then isolated using density gradient centrifugation. Lymph nodes, thymus and spleen were homogenized to generate single cell suspensions. Splenocytes were subjected to red blood cell lysis before staining. Peripheral blood and bone marrow were also incubated with lysis buffer to lyse contaminating erythrocytes. For isolation of cells from intestine and colon, intestines were excised from animals, fat was removed and the intestines were flushed. Peyer's patches were removed from the small intestine and organs were cut into pieces of approximately 1 cm length. Mucus was removed by incubating in HBSS containing 5 mM DTT, 2% FCS, 100 U/ml Penicillin and 100 μg/ml Streptomycin in a shaking incubator at 37°C, 200 rpm for 20 min. To remove epithelial cells, intestines were then washed 3 times for 15 min each in HBSS containing 5 mM EDTA, 2% FCS, 100 U/ml Penicillin and 100 μg/ml Streptomycin in a shaking incubator at 37°C, 200 rpm. To remove FCS and EDTA, tissue was then transferred into HBSS containing 10 mM HEPES, 100 U/ml Penicillin and 100 μg/ml Streptomycin and incubated in a shaking incubator at 37°C, 200 rpm for 10 min. Tissues were then minced and transferred into HBSS containing 0.2 U/ml Liberase (Roche), 200 U/ml DNase (Roche), 10 mM HEPES, 100 U/ml Penicillin and 100 μg/ml Streptomycin. Digestion was carried out in a shaking incubator at 37°C, 200 rpm for 45 min. The reaction was stopped by addition of EDTA containing buffer and cells were filtered through 70 μm sieve. To isolate cells from the skin, a 2 cm^2 area of skin from the trunk of the animals was depilated, excised and lightly defatted. The tissue was minced and then digested in a shaking incubator at 37°C, 150 rpm for 90 min in PBS containing 0.8 U/ml Liberase (Roche) and 200 U/ml DNase I (Roche). After digestion, a single cell suspension was generated by gently pipetting up and down and filtered through a 70 μm cell strainer.

Purification of Human T Cells

Human CD4$^+$ T cells were purified by negative selection using CD4-RosetteSep (Stem Cell) or positive selection using CD4 pluribeads (Pluriselect) according to manufacturer's instructions. To isolate Treg (CD3$^+$CD4$^+$CD25$^+$CD127$^-$), Tconv (CD3$^+$CD4$^+$CD25$^-$CD127$^+$), naive (CD3$^+$CD4$^+$CD25$^-$CD127$^+$CD45RA$^+$), and memory T cells (CD3$^+$CD4$^+$CD25$^-$CD127$^+$CD45RA$^-$), this was followed by positive-selection using CD25-specific MACS beads (Miltenyi Biotech) or sorting on a BD Aria III cell sorter (Becton Dickinson) after incubating cells with combinations of fluorochrome-labeled monoclonal antibodies against CD3, CD4, CD45RA, CD25,

and CD127. To exclude dead cells, cells were stained with LIVE/DEAD fixable near-IR dead cell stain kit (Thermo Fisher Scientific). For experiments with non-sorted cells, only samples with > 95% purity were used.

Generation of iTreg Cells, Differentiation of TH cells, and Stimulation and Inhibition of Human and Murine T Cells

Human $CD4^+$ lymphocytes were purified from whole blood of healthy human donors by negative selection using CD4-RosetteSep (Stem Cell). After negative selection with CD25-specific MACS beads (Miltenyi Biotech), conventional $CD4^+$ T cells were incubated with CD45RA-specific MACS beads (Miltenyi Biotech). Naive conventional T cells were obtained by passing the cell mixture over LS magnetic separation columns in a MidiMACS (Miltenyi Biotech) and collecting the $CD4^+CD25^-CD45RA^+$ T cells. Naive (Treg-cell depleted) $CD4^+$ T cells (5×10^4 cells/well) were stimulated with 5×10^4 magnetic beads coated with 5% CD3 (OKT3, Ortho Biotech), 12% CD28 (9.3), and 83% anti-MHC-I (W6/32) monoclonal antibody per well (CD3-CD28-MHC-I beads) and 10 ng/ml TGF-β (Peprotech) added for a period of 5 days in the presence of IL-2 (300 U/ml) for the generation of iTreg cells. For differentiation of TH1, TH2, TH9, and TH17 cells, naive T cells were stimulated in the presence of 10 ng/ml IL-12 and 10 U/ml IL-2 (TH1), 20 ng/ml IL-4 (TH2), 20 ng/ml IL-4 and 1 ng/ml TGF-β (TH9), and 25 ng/ml IL-21 and 5 ng/ml TGF-β (TH17) (Klotz et al., 2009). For stimulation of human Tconv, Treg, TH, and iTreg cells, cells were incubated with PGE_2 (1 μM), IL-2 (0.5-1,000 U/ml), IL-2/PGE_2 (20 U/ml, 1 μM), soluble CD3 (1.0 μg/ml), CD3 beads (3:1), soluble CD28 (5 μg/ml), IL-2/soluble CD3 (20 U/ml, 1.0 μg/ml), IL-2/CD3 beads (20 U/ml, 3:1), CD3-CD28-MHC-I beads (3:1), and IL-2/CD3-CD28-MHC-I beads (20 U/ml, 3:1) for 12-72 hr as indicated. For inhibition of IL-2 signaling Treg cells were incubated with increasing doses of Janex-1 (JAK3, Cayman Chemicals), STAT5 inhibitor (STAT5, Merck), and PD98059 (MEK, Merck). Viability of Treg cells was routinely monitored using Annexin-V/PI staining. For analysis of PPARγ dependency of HPGD expression, human and murine Tconv and Treg cells were incubated with 1 μM pioglitazone (Cayman Chemicals) or 15-keto-PGE_2 (Cayman Chemicals) or rosiglitazone (Cayman Chemicals) overnight. For IL-33 stimulation, cells were cultivated overnight on plates coated with 10 ng/ml CD3 (BioLegend) and stimulated with 2 μg/ml CD28 (BioLegend) and 1000 U/ml IL-2 (Proleukin, Novartis). Cells were then stimulated with 10 ng/ml IL-33 (BioLegend) for 45 min before harvesting.

qRT-PCR

Cells were resuspended in TRIZOL (Thermo Fisher Scientific) and total RNA was isolated according to manufacturer's recommendations. If fewer than 5,000 cells were used for RNA isolation, the miRNeasy Mini Kit (QIAGEN) was used instead. cDNA was generated from the isolated RNA with the Transcriptor First Strand cDNA synthesis kit (Roche Diagnostics). qRT-PCR was performed using either SYBR Green (Roche) or the LightCycler Taqman master kit and the Universal Probe Library assay (Roche Diagnostics) according to manufacturer specifications. Primers and probes used are listed in Table S7. Results were normalized to housekeeping genes (β-actin for murine and B2M for human samples).

Immunoblot Analysis

Immunoblotting was performed as previously described (Beyer et al., 2011). Cell lysates from purified human Tconv and Treg were generated by lysing in RIPA buffer (10 mM Tris-Cl (pH 8.0), 1 mM EDTA, 0.5 mM EGTA, 1% Triton X-100, 0.1% sodium deoxycholate, 0.1% SDS, 140 mM NaCl) supplemented with cOmplete Protease Inhibitor (Roche) for 30 min on ice before spinning at maximum speed for 10 min at 4°C. The protein-containing supernatant was collected for further processing. To isolate protein from whole organs, tissue was transferred into digestion buffer containing 50 mM Tris-HCl, 1 mM EGTA, 1 mM EDTA, 10 mM β-Glycerolphosphate, 50 mM Sodium Flouride, 5 mM Sodium Pyrophosphate, 1 mM Sodium Vanadate, 270 mM Sucrose, 1% Triton and supplemented with cOmplete Protease Inhibitor (Roche) and PhosSTOP (Roche). Tissues were minced using GentleMacs M Tubes (Miltenyi Biotec) and incubated on ice for 30 min to allow for sufficient lysis. Lysates were then centrifuged at maximum speed for 10 min at 4°C and the fat layer was removed before transferring the supernatant to a new tube and repeating the centrifugation as necessary until no fat remnants or pellets remained. If AKT phosphorylation was analyzed, animals were challenged with 0.5 U/kg bodyweight of insulin i.p. 3 min prior to euthanasia.

Lysates were run on 10% - 14% SDS-PAGE gels depending on the size of target proteins and blotted onto nitrocellulose membranes. Blotting was performed at RT for 30 min in 5% Milk in PBST (PBS supplemented with 0.01% Tween-20). Primary antibody incubation was performed in 5% Milk in PBST or 2.5% BSA in PBST, according to the manufacturers' recommendations for at least 12 hr at 4°C. Blots were incubated with secondary antibodies coupled to HRP at RT for 1.5 hr. Detection was performed using enzymatic chemiluminiescence (ECL) detection reagent (Sigma-Aldrich) and imaged using a Chemidoc (Biorad). Quantification was performed using Image Studio. The following antibodies were used: HPGD antibody (kind gift of R. Balderas, BD Biosciences), pAKT (Cell Signaling Technology), AKT (Cell Signaling Technology), FABP4 (Cell Signaling Technology, 2120S), PPARγ (Cell Signaling Technology), UCP1 (Thermo Fisher Scientific), as well as beta-actin (Millipore) and Calnexin (Calbiochem) as loading controls.

Whole Transcriptome Analysis in Human Cells

Generation and analysis of human gene expression data from Treg and Tconv cells has been previously described (Beyer et al., 2011). Briefly, Treg-cell specific genes showing a high correlation to FOXP3 expression were identified in a multi-step process: 1. fold-changes between unstimulated, freshly isolated Treg and Tconv cells were calculated and differentially expressed genes (FC > |2.0|, p value < 0.05, FDR-corrected) were further analyzed; 2. Fold changes for all other conditions and T cell subsets were calculated against Tconv cells as reference for these genes; 3. Only genes which did not show differential expression in any of the other comparisons were further included in the analysis. This resulted in a set of 25 genes including FOXP3 which were

differentially expressed between Treg and Tconv cells but not in the other comparisons and showed positive correlation with FOXP3 expression in the dataset.

Chromatin Immunoprecipitation, Whole Genome Arrays, ChIP qPCR, and Electromobility Shift Assays

Chromatin immunoprecipitation (ChIP) for FOXP3 and STAT5 has been previously described (Beyer et al., 2011). ChIP was performed on human Treg and Tconv cells stimulated with IL-2 before cross-linking for 10 min in 1% formaldehyde solution. Cell lysis, ChIP and DNA isolation steps were carried out as previously described (Sadlon et al., 2010). Briefly, cells were lysed in lysis buffer 1 (50 mM HEPES-KOH, pH 7.5, 140 mM NaCl, 1 mM EDTA, 10% glycerol, 0.5% NP-40, 0.25% Triton X-100, 1 × protease inhibitors). After centrifugation, pellets were further lysed in lysis buffer 2 (10 mM Tris-HCl, pH 8.0, 200 mM NaCl, 1 mM EDTA, 0.5 mM EGTA, 1 × protease inhibitors). Pellets were then resuspended in lysis buffer 3 (10 mM Tris-HCl, pH 8.0, 100 mM NaCl, 1 mM EDTA, 0.5 mM EGTA, 0.1% Na-Deoxycholate, 0.5% *N*-lauroylsarcosine, 1 × protease inhibitors) for sonification. Sonification consisted of 12 repeats of 30 s pulses with an amplitude of 90% with 90 s between pulses. For immunoprecipitation, sonicated samples were incubated with beads coated with a goat STAT5 antibody or a corresponding IgG control (C-17X, Santa Cruz) overnight at 4°C. Beads were then washed with RIPA followed by another wash-step in TE containing 50 mM NaCl before eluting the bound chromatin in elution buffer (50 mM Tris-HCl, pH 8.0, 10 mM EDTA, 1.0% SDS) at 65°C for 15 min. Reverse crosslinking was performed by incubating at 65°C for another 6 hr. RNase A digestion was carried out at 37°C for 2 hr, followed by Proteinase K digestion at 55°C for another 2 hr. Chromatin was then isolated using the QIAquick PCR Purification kit (QIAGEN).

Validation of FOXP3 and STAT5 binding to genomic regions was carried out by ChIP-qPCR. Reactions were performed using either the Maxima SYBR Green qPCR master mix (STAT5, Thermo Fisher Scientific) or RT2 SYBRgreen/ROX qPCR master mix (FOXP3, SABiosciences). The relative enrichment of target regions in STAT5 or FOXP3 immunoprecipitated material relative to input chromatin analysis was carried out using the 2-ΔΔCT method. Immunoprecipitations using goat or rabbit IgG were used to normalize for non-specific background. PCR primer sequences are listed in Table S7. EMSA were performed with fluorescent-dye conjugated oligonucleotides with His-tagged FOXP3 protein according to the manufacturer's recommendations (LI-COR) and analyzed with the Odyssey infrared imaging system following electrophoresis (Table S7). For supershift assays an anti-His antibody (ab9108) or rabbit IgG was added to the reaction.

For bioinformatics analysis, the false discovery rate (FDR) was set to 0.5%. Gene accessions were assigned if the enriched peak was located between 20kb upstream of the transcription start site (TSS) and 20kb downstream of the end of transcription as described previously (Sadlon et al., 2010).

Cloning of HPGD Constructs with Potential FOXP3 and STAT5 Binding Regions

To assess regulation of HPGD expression by binding of FOXP3 and STAT5, the corresponding HPGD genomic regions were amplified by PCR using human genomic DNA as source material. The HPGD promoter and the FOXP3 binding region sequences were amplified with the primers listed in Table S7. After digestion with Xho I and BglII for the HPGD promoter resp. Nhe I and Hind III for Foxp3 BR 1 and 2, the fragments were cloned into the pGL4.24 vector with a minP element upstream of the potential binding motif and a destabilized downstream Firefly luciferase.

Luciferase Assays

To assess binding of STAT5 to the promoter of HPGD, the HPGD promoter constructs or a control construct as well as a plasmid encoding renilla luciferase for normalization were transfected into Jurkat cells in 96-well plates as described previously (Beyer et al., 2016) and incubated with IL-2 and a STAT5 inhibitor (N'-((4-Oxo-4H-chromen-3-yl)methylene)nicotinohydrazide, Merck Darmstadt). To assess regulation of HPGD expression by binding of FOXP3 to the genomic locus of HPGD, the respective constructs were transfected separately into HEK293T cells in 96-well plates together with a control plasmid. Lysis and analysis were performed 24 h post-transfection using the Promega Dual Luciferase Kit. Luciferase activity was counted in a Mithras plate reader (Berthold).

Enzymatic Activity of HPGD

The enzymatic activity of HPGD was assessed in human Treg and Tconv cells, which were stimulated for 24 hr with IL-2. The enzymatic activity was determined using a radioactive assay that measures the transfer of ^{3}H from 15(S)-[15-^{3}H]PGE_2 to glutamate by coupling HPGD with glutamate dehydrogenase. Metabolization of PGE_2 by IL-2 stimulated human Treg and Tconv cells was assessed after 24 hr of incubation using the Prostaglandin E Metabolite EIA Kit (Cayman Chemicals). The ability of HPGD to convert PGE_2 into 15-keto-PGE_2 was assessed in human Treg and Tconv cells, which were stimulated for 24 hr with IL-2 and PGE_2. The enzymatic activity was determined using LC-MS/MS as previously described (Schmitz et al., 2014). Briefly, homogenized tissue pieces were extracted by liquid-liquid extraction and samples were spiked with internal standards. For chromatography, samples were injected into a linear gradient consisting of a water/formic acid (100:0.0025) mobile phase A and an acetonitrile/formic acid (100:0.0025) mobile phase B at a flow rate of 300 μl/min. Negative ion electrospray mass spectrometry was performed. Quantification was done by multiple reaction monitoring.

Inhibition of T cell Proliferation

CFSE or eFluor 670-labeled (both eBioscience; labeling according to manufacturer's instructions) human or murine $CD4^+$ T cells or $CD4^+CD25^-$ Tconv cells (1 × 10^5 cells/well) were stimulated in the presence of CD3-CD28-MHC-I or CD3-CD28-coated magnetic

beads respectively (3×10^5 beads/well) in 96-well plates in RPMI supplemented with 10% FCS with increasing amounts of the 15 s stereoisomers of PGE_2, $PGF_{2\alpha}$, PGD_2, PGJ_2 or the PGE_2-metabolite 15-keto-PGE_2 (all from Cayman Chemicals) for 72 hr. CFSE or eFluor 670 dilution was measured on a BD LSR II flow cytometer.

In Vitro Suppression Assays Using Treg Cells

For *in vitro* suppression assays, CFSE or eFluor 670-labeled (both eBioscience; labeling according to manufacturer's specifications) human or murine $CD4^+CD25^-$ Tconv cells (1×10^5 cells/well) were co-cultured with Treg cells or lentivirally transduced Tconv cells at indicated ratios in the presence of CD3-CD28-MHC-I or CD3-CD28-coated magnetic beads respectively (1.0×10^5 beads/well) in 96-well plates in RPMI or X-Vivo 15 (Lonza) supplemented with 10% FCS (Sigma Aldrich) and Glutamax (Thermo Fisher Scientific) for 72 hr with or without PGE_2, $PGF_2\alpha$, PGD_2, PGJ_2 or the PGE_2-metabolite 15-keto-PGE_2 at the indicated concentrations. For transwell assays, Treg cells and PGE_2 were added to the upper chamber while Tconv cells and beads were added to the lower chamber. CFSE or eFluor 670 dilution was measured on a BD LSR II flow cytometer.

RNA Isolation, Library Preparation, Sequencing, and Bioinformatic Analysis

Total RNA from Tconv and Treg cells from male $Foxp3^{Cre}$ and $Foxp3^{Cre}HPGD^{fl/fl}$ animals was extracted with QIAzol Lysis Reagent (QIAGEN) and then purified using the miRNeasy Mini Kit (QIAGEN) according to the manufacturer's recommendations. The RNA integrity (RNA Integrity Score $\geq$ 6.8) and quantity were determined on the Agilent 2100 Bioanalyzer (Agilent) per manufacturer's recommendation and further processed. Purification of mRNA was performed using polyT oligo attached magnetic beads. Following the purification, the mRNA was used for library preparation using TruSeq RNA Sample Prep Kit v2 (Illumina). Sequencing was carried out on an Illumina HiSeq1500 using 100 bp single-read sequencing. RNA-seq reads were aligned against the murine reference genome mm10 using TopHat v2.0.11. To obtain transcript and gene information, aligned reads were mapped against the mm10 RefSeq database using Partek Genomics Suite (PGS) software (v6.6; Partek Inc.). Annotated data were normalized using the DESeq2 package within the statistical software R version 3.0.2. Additionally, normalized read counts lower than 1 were set equal to 1 to avoid spurious fold changes later on. The genes were filtered to those being present within the dataset, defined as having a mean normalized read count larger than 10 in at least one of the investigated groups. Of those, the genes being variable ($p < 0.05$) across the dataset were visualized via t-distributed stochastic neighbor embedding (t-SNE) (van der Maaten and Hinton, 2008). Next, using a previously published Treg-cell signature (Hill et al., 2007), we compared transcriptomes of $Foxp3^{Cre}$ and $Foxp3^{Cre}HPGD^{fl/fl}$ Treg cells with the respective Tconv cells. To identify genes specifically changed in $Foxp3^{Cre}HPGD^{fl/fl}$ Treg cells, we selected genes, that were up- or downregulated (> 2-fold) in gene expression profiles of $Foxp3^{Cre}$ and $Foxp3^{Cre}HPGD^{fl/fl}$ Treg cells compared with their corresponding Tconv cells. These gene sets were further filtered by taking only the genes that were > 1.5-fold up- or downregulated in $Foxp3^{Cre}HPGD^{fl/fl}$ Treg cells compared with $Foxp3^{Cre}$ Treg cells. These 210 $Foxp3^{Cre}HPGD^{fl/fl}$ Treg-cell signature genes were visualized in form of a heatmap based on z-transformed data. Finally, all 210 $Foxp3^{Cre}HPGD^{fl/fl}$ Treg-cell signature genes were linked to prior knowledge by performing Gene Ontology Enrichment Analysis (GOEA) using the Cytoscape plug-in BiNGO (v2.44) with an FDR threshold of 0.05 to include only significant results. The Cytoscape plugins Enrichment Map (v1.1) with a Jaccard coefficient of 0.25 and an FDR Q-value cutoff of 0.1 as well as Word Cloud were used to visualize the GO network.

Analysis of VAT Treg Cells by SmartSeq2

Treg cells from the VAT of $Foxp3^{Cre}HPGD^{fl/fl}$ or $Foxp3^{Cre}HPGD^{fl/wt}$ animals were isolated as described above. Total RNA was isolated using the miRNeasy Mini Kit (QIAGEN) and transcriptome analysis was performed by SmartSeq2 (Picelli et al., 2013). Per sample, 500 pg RNA was denatured for 2 min at 95°C in 0.1% Triton X-100 containing 0.05 mM dNTP, 2 μM anchored oligodT (Smart dT30VN) primer and 1 U/μl RNase Inhibitor (Takara). Reverse transcription was carried out at 42°C for 90 min followed by 15 min inactivation at 70°C using 5 U/μl Superscript II reverse transcriptase (Thermo Fisher Scientific) in 1X Superscript II Buffer supplemented with 5 mM DTT, 1 M Betaine, 14 mM $MgCl_2$, 1 μM Template Switching Oligo and 1 U/μl RNase Inhibitor. cDNA was then pre-amplified using KAPA HiFi HotStart ReadyMix (Kapa Biosystems) containing 1 nM ISPCR Primer. Amplification was carried out for 16 cycles consisting of 20 s denaturation at 98°C, 20 s annealing at 67°C and 6 min elongation at 72°C each after an initial denaturing at 98°C for 3 min. The pre-amplification reaction was then purified by using a 0.8:1 ratio of AMPure XP beads (Beckman Coulter). DNA was allowed to bind to beads for 3 min at RT followed by one wash in 80% Ethanol for 30 s. cDNA was then eluted from the beads in 15 μl of water before checking for cDNA quality on a Tapestation 2200 using a HighSensitivity D5000 assay (Agilent Genomics) according to manufacturer's instructions. Tagmentation, PCR amplification and indexing of samples was performed using the Nextera XT DNA Library Preparation Kit (Illumina) according to manufacturer's recommendations. After library preparation, DNA was purified with a 1:1 ratio of AMPure XP beads and sample. Quantification and quality check of libraries was done on a Tapestation 2200 using a HighSensitivity D5000 Assay. Library concentrations were adjusted to 2nM and pooled prior to sequencing SR 75 bp with two 8 bp index reads on an Illumina NextSeq 500 instrument using High Output v2 chemistry. RNA-seq data was demultiplexed using bcl2fastq2 v2.20 and pseudo aligned to Mus_musculus.GRCm38.cdna.all.fa.gz transcriptome using kallisto v.0.44.0. The sequences of all oligos used for SmartSeq2 can be found in Table S7. All oligos were biotinylated at the 5′ end to avoid the formation of concatamers. To identify genes specifically changed in $Foxp3^{Cre}HPGD^{fl/fl}$ Treg cells, we identified genes, that were up- or downregulated between $Foxp3^{Cre}$ and $Foxp3^{Cre}HPGD^{fl/fl}$ Treg cells (FC > |2.0|, p value < 0.05, FDR-corrected). This gene set was further filtered by a) excluding genes not differentially expressed $Foxp3^{Cre}$ Treg cells and Tconv cells for genes downregulated in HPGD-deficient Treg cells and b) excluding genes not differentially expressed $Foxp3^{Cre}HPGD^{fl/fl}$ Treg cells and Tconv cells for genes

upregulated in HPGD-deficient Treg cells. These 101 Foxp3^{Cre}HPGD$^{fl/fl}$ Treg-cell signature genes were visualized in form of a heatmap based on z-transformed data.

Single-Cell Real Time PCR

Single Treg cells were double-sorted by flow cytometry into individual wells of a 96-well plate containing 5 μL of 0.2% Triton X-100 and 0.4 U/ml RNase inhibitor. RT pre-amplification was performed on 24 single cells of each type. Each well was supplemented with 0.1 μL of SuperScript III RT/Platinum Taq (Thermo Fisher Scientific), 6 μL of 2x reaction mix and a mixture of primer pairs for HPGD, Foxp3, Pparg, B2m, and Gapdh genes (100 nM final concentration; Table S7). Single-cell mRNA was directly reverse transcribed into cDNA (50°C for 15 min, 95°C for 2 min), pre-amplified for 15 cycles (each cycle 95°C for 15 s, 60°C for 1 min) and cooled at 4°C for 15 min. Samples were then diluted 1:10 with 10 mM Tris-HCl, pH 8. Real-Time PCR analysis was performed for each gene separately with the same set of primers used for the RT preamplification stage (400 nM final concentration) using Maxima SYBR Green qPCR master mix (Thermo Fisher Scientific) on a LightCycler 480 II (Roche Diagostics). Quantification was performed as relative to the average of all cells for a given gene (n = 21), using the 2-ΔΔCT method, where Ct is the mean qPCR cycle threshold signal of two replicate qPCR reactions per cell and normalized to B2m expression.

Induction and Assessment of Colitis

For DSS-induced colitis, DSS (MP Biochemicals) with a molecular weight of 36–50 kDa was dissolved in distilled water to provide a working solution of 5% (weight/volume). To induce colitis, female Foxp3^{Cre}HPGD$^{fl/fl}$ or Foxp3^{Cre}HPGD$^{fl/wt}$ mice were given free access to this solution for 6 days whereupon DSS was replaced with normal water. Mice were weighed daily and inspected for clinical signs of disease.

For adoptive transfer experiments, splenocyte samples were enriched for CD4$^+$ T cells by negative selection on MACS columns with the CD4$^+$ T cell isolation kit II (Miltenyi Biotec). Cells were then stained for CD44, CD62L, CD25, CD4, CD8α, and CD3 and naive CD4$^+$CD25$^-$CD44$^-$CD62L$^+$YFP$^-$ T cells were sorted on a BD Aria III. Inflammatory bowel disease was induced by the adoptive transfer of 1 × 10^6 naive CD4$^+$CD25$^-$CD44$^-$CD62L$^+$YFP$^-$ T cells that were purified from Foxp3^{Cre}HPGD$^{fl/wt}$ mice into *Rag2*$^{-/-}$ animals by tail vain injection. Mice that received 2.5 × 10^5 CD4$^+$YFP$^+$CD25$^+$ Treg cells from Foxp3^{Cre}HPGD$^{fl/wt}$ mice at the same time as the naive CD4$^+$CD25$^-$CD44$^-$CD62L$^+$YFP$^-$ T cells served as controls. To test the function of HPGD-deficient Treg cells, mice received 2.5 × 10^5 CD4$^+$YFP$^+$CD25$^+$ Treg cells from Foxp3^{Cre}HPGD$^{fl/fl}$ mice together with the naive CD4$^+$CD25$^-$CD44$^-$ CD62L$^+$YFP$^-$ T cells. Recipient mice were weighed 3 times per week and monitored for signs of illness. 6 weeks after transfer the animals were sacrificed.

To determine Treg-cell suppressive efficacy *in vivo*, the mesenteric lymph nodes as well as spleens were analyzed by flow cytometry. For histological analysis, the large intestine (from the ileocecocolic junction to the anorectal junction) was removed, colon length determined, subsequently washed and fixed in 4% buffered formalin solution, and routinely processed for histological examination. Sections were stained with hematoxylin and eosin and assigned scores as described previously (ten Hove et al., 2002). Briefly, scores were assigned from 0 – 3 in 5 different categories: (1) number of follicle aggregates, (2) edema, (3) erosion and ulceration, (4) crypt loss and (5) infiltration of mono- and polymorphonuclear cells. Furthermore, the (6) percentage of the involved area was assigned a score from 0 – 4. All scoring was performed by researchers blinded to the experimental conditions.

To determine cell intrinsic versus extrinsic functionality of HPGD, 1.5 × 10^5 CD3$^+$CD4$^+$RFP$^+$ Treg cells and 1 × 10^6 CD3$^+$CD4$^+$CD44$^-$CD62L$^+$RFP$^-$ naive T cells isolated from Foxp3-IRES-RFP mice were injected with 1 × 10^5 CD3$^+$CD4$^+$YFP$^+$ Treg cells isolated from either Foxp3^{Cre}HPGD$^{fl/fl}$ or Foxp3^{Cre}HPGD$^{fl/wt}$ animals into *Rag2*$^{-/-}$ animals as described above. Mice receiving only 1 × 10^6 CD3$^+$CD4$^+$CD44$^-$CD62L$^+$RFP$^-$ naive T cells served as controls. After 6 weeks, the animals were sacrificed and CD3$^+$CD4$^+$YFP$^+$ Treg cells were sorted from mesenteric lymph nodes and the transcriptional profiles of the isolated Treg cells analyzed by SmartSeq2 as described above to identify differentially expressed genes (FC > |2.0|, p value < 0.05, FDR-corrected) between Foxp3^{Cre}HPGD$^{fl/fl}$ and Foxp3^{Cre}HPGD$^{fl/wt}$ Treg cells after homeostatic expansion *in vivo*. Mean gene expression was plotted against fold-change for all genes. Next, Treg-cell signature genes were visualized in form of a heatmap based on z-transformed data.

Bisulphite Sequencing

Genomic DNA from human Treg and Tconv cells purified by negative selection using CD4-RosetteSep (Stem Cell), followed by sorting on an BD Aria III cell sorter after incubating cells with a combination of fluorochrome-labeled monoclonal antibodies to CD3, CD4, CD25, and CD127 was isolated using phenol/chloroform extraction. Sodium bisulphate treatment of genomic DNA was performed resulting in the deamination of unmethylated cytosines to uracil, whereas methylated cytosines remain unchanged (Beyer et al., 2011). After amplification PCR products were purified and sequenced in both directions by pyrosequencing. PCR primer sequences are listed in Table S7.

Expansion of Human Treg Cells

CD4$^+$CD25^{hi}CD127^{lo}CD45RA$^-$ and CD4$^+$CD25^{hi}CD127^{lo}CD45RA$^+$ Treg cells as well as CD4$^+$CD25$^-$CD127$^+$CD45RA$^+$ Tconv cells were isolated on a BD Aria III and plated at 2.5 × 10^5 Treg or Tconv cells per well in a 24-well plate and activated with CD3-CD28-coated microbeads (Thermo Fisher Scientific) at a 3:1 bead to cell ratio. Cultures were grown in the presence of IL-2 throughout the expansion period (300 IU/ml, Proleukin). Cells were resuspended and fresh media and IL-2 (300 IU/ml) added at days 5, 7, 9, and 12 assuming consumption of IL-2. On day 8, cells were restimulated with fresh CD3-CD28-coated beads. Cultured

cells were harvested at day 14 for analysis by flow cytometry, mRNA analysis as well as analysis of histone modifications (only cultures with > 95% FOXP3 expression were used for further studies).

Gene-Specific mRNA Silencing

All siRNAs were purchased from Biomers and used for transfection of freshly isolated primary human Treg cells. Transfection was carried out with the human T cell nucleofector kit (Lonza) as per manufacturer's recommendations as previously described (Beyer et al., 2011) and gene expression and suppressive activity determined as described above. Sequences are listed in Table S7.

Immunohistochemical Analysis of VAT Macrophages

For histological examination and enumeration of macrophages in VAT, paraffin sections with a diameter of 5μm were stained for F4/80. Sections were incubated with rat anti-mouse F4/80 antibody (Abcam) diluted 1:50 at 4°C overnight. The sections were then incubated with biotin-labeled polyclonal rabbit anti-rat IgG (Thermo Fisher Scientific) for 30 min. Finally, slides were incubated with streptavidin-conjugated horseradish peroxidase for another 30 min followed by a 10 min incubation in the chromogen amino-ethyl carbazole. Nuclei were counterstained with hematoxylin. Macrophages were counted and their size was determined using CellProfiler 2.0. All samples were enumerated by researchers 'blinded' to the experimental conditions.

Analysis of Prostaglandins in Colonic Tissue and Serum

LC-MS/MS was used for the quantitation of prostanoids from colonic tissue and serum of mice after DSS treatment or transfer of T_{naive} cells into *Rag2*$^{-/-}$ animals as described above (Schmitz et al., 2014).

Assessment of Histone Modifications in Human CD4^{+} T Cells

ChIP experiments were performed as previously described (Beyer et al., 2011). In brief, expanded Treg and Tconv cells were harvested on day 14, treated with MNase to generate approximately 80% mononucleosomes and 20% dinucleosomes. Chromatin from 2.5 × 10^{6} cells was used for each ChIP experiment, which yielded approximately 1000 pg of DNA. Antibodies against histone H4Ac (17-630), H3K4me3 (17-614) and H3K27me3 (17-622; Millipore) as well as an isotype control antibody were used. Multiplex DNA libraries were generated using the ChIP-Seq Sample Preparation Kit (Illumina) and the Multiplexing Sample Preparation Oligonucleotide Kit (Illumina) following the manufacturer's instructions. Purified DNA ends were repaired using PNK and Klenow enzyme, followed by treatment with Klenow exo minus polymerase to generate a protruding 3′ Adenine used for adaptor ligation. Next, size selection of libraries was performed as follows: DNA libraries were agarose gel purified, DNA fragments with approximately 220 bp size excised and eluted using QIAquick Gel Extraction kit (QIAGEN). After subsequent adaptor ligation to the repaired ends, an amplification step was performed for 5 cycles with PCR primers 1.1 and 2.1 (Illumina). During a second amplification step (13 cycles) multiplex PCR primers were added to the DNA libraries to construct multiplex sequencing libraries. DNA libraries were sequenced with an Illumina HiScan SQ in a multiplex single-read run with at least 40 bases sequencing length and 6 bases for index sequences. Sequence reads from each DNA library were aligned with Casava software (Illumina) against the human reference genome 18 (NCBI 36/hg18), converted into the .bam file format and visualized. To confirm histone modifications observed at the HPGD locus in human expanded Treg cells, previously published human genome-wide data were used to extract HPGD histone methylation in Tconv and Treg cells (Bernstein et al., 2010).

Metabolic Studies

Metabolic studies were performed with mice of 6-10 weeks, 12-20 weeks or > 40 weeks of age; mice were fasted for 14 hr overnight, weighed and then tested for fasting blood glucose concentrations (Accu Chek Aviva, Roche). We performed glucose tolerance tests (GTTs) and insulin tolerance tests (ITTs). For GTTs, glucose (2.0 g per kg bodyweight) was administered by intraperitoneal (i.p.) injection after an overnight fast. Blood glucose levels were measured before and 15, 30, 60, 120 and 240 min after glucose injection. For ITTs, insulin (1 IU/kg bodyweight, Humulin R, Lilly) was administered by i.p. injection after 4 hr of fasting. Blood glucose levels were measured before and 20, 40, 60, 80, 100 and 120 min after insulin injection. To determine blood insulin levels, blood was drawn and serum separated by centrifuging at 1000 g for 10 min in serum tubes (Sarstedt). Insulin ELISA (Ultrasensitive Mouse Insulin ELISA, Mercodia) was performed in 96-well half-area plates (Greiner) according to the manufacturer's instructions.

Analysis of HPGD Expression in Human T2D Patients

Approximately 25 mL blood was drawn from healthy controls and T2D patients in heparinized tubes and shipped overnight for further processing. 1 mL blood was removed from the tubes and stained for CD3, CD4, CD25, CD127 and FoxP3. Countbright Counting Beads (eBioscience) were added to allow for subsequent quantification and samples were acquired on a BD LSR II. The remaining sample was stained for CD3, CD4, CD25, CD127 and sorted for Treg (CD3+CD4+CD25+CD127-) and Tconv cells (CD3+CD4+CD25-CD127+). Sorted cells were resuspended in TRIZOL, RNA isolated and cDNA synthesis performed with subsequent qPCR as described above.

Generation of Human Macrophages and DCs

Human monocytes were purified from peripheral blood mononuclear cells by MACS using CD14 beads in accordance with the manufacturer's instructions. Cells were differentiated into macrophages and dendritic cells. To generate macrophages, cells were

stimulated with 500 U/ml GM-CSF for 72 hr. To differentiate cells into DCs, cells were stimulated with 500 U/ml IL4 and 800 U/ml GM-CSF for 6 days. To analyze the effect of 15-keto-PGE_2 and rosiglitazone on DC differentiation, 1 μM 15-keto-PGE_2, rosiglitazone or DMSO as vehicle control were added to the differentiation medium at day 3. CD14 and CD86 expression on these cells as an indicator of their differentiation state were analyzed by flow cytometry on day 6.

Isolation and Stimulation of B Cells from Human Buffy Coats

B cells were isolated from Buffy coats using the MagniSort Human CD19 Positive Selection Kit (eBioscience) according to manufacturer's specifications and purity was determined by flow cytometry. Cells were then stimulated for 24 hr with 1 μM 15-keto-PGE_2 or 5 μM rosiglitazone before staining for viability with Annexin V/PI.

Isolation and Stimulation of NK Cells from Human Buffy Coats

NK cells were isolated from Buffy coats using the MojoSort Human NK Cell Isolation Kit (BioLegend) according the manufacturer's specifications and purity was determined by flow cytometry. Cells were stimulated with 300 U/ml IL-2 for 1 hour before adding 1 μM 15-keto-PGE_2 or rosiglitazone for another 6 hr stimulation. Cells were then harvested in TRIZOL, RNA isolated and cDNA synthesis performed before analyzing IFN-γ expression by qPCR.

Generation of Murine BMDMs

Femur and tibia were removed from mice and briefly dipped in 70% Ethanol to sterilize the bones. The ends of the bones were cut off and bone marrow was flushed out with DMEM. Marrow was centrifuged at 300 g for 8 min and red blood cells were lysed.

For BMDM differentiation, cells were cultivated in DMEM containing 10% FCS and 20 ng/ml rmM-CSF. After 3 days, the medium was refreshed before being replaced with DMEM containing 10% FCS after 6 days of cultivation. Cells were then stimulated with 1 μM 15-keto-PGE_2 or rosiglitazone overnight and resuspended in TRIZOL. RNA was isolated and cDNA synthesis performed with subsequent qPCR for Angptl4 as described above.

Isolation of Myeloid Populations from Murine Spleens

Mice were sacrificed by cervical dislocation and spleens were excised. Spleens were digested at 37°C for 45 min with 10 mM HEPES, 0.5 mg/ml Collagenase Type IV (Sigma Aldrich) and 0.05 mg/ml DNase I (Sigma Aldrich) in RPMI medium. Red blood cell lysis was performed and cells were stained with LIVE/DEAD fixable near-IR dead cell dye (Thermo Fisher Scientific), lineage markers (CD3, B220, NK1.1, CD19) and CD11b, Ly6G, CD11c and F4/80. Cells were then sorted on a BD Aria III into dendritic cells ($live^-lin^-CD11b^+CD11c^+$), granulocytes ($live^-lin^-CD11b^+CD11c^-Ly6G^+$), red pulp macrophages ($live^-lin^-CD11b^{int}F4/80^+$), and marginal zone macrophages ($live^-lin^-CD11b^{hi}F4/80^+$). Sorted cells were resuspended in TRIZOL, RNA isolated and cDNA synthesis performed with subsequent qPCR as described above.

Differentiation and Stimulation of 3T3-L1 Cells

Cells were grown to 100% confluence and kept as a confluent culture for 48 hr before stimulation with 1 μM Dexamethasone, 0.5 mM Methylisobutylxanthine (IBMX) and 1 μg/ml bovine Insulin (Sigma Aldrich) in DMEM with 10% FCS. After 48 hr, the stimulus was removed and cells were cultured for 6 days in DMEM containing 10% FCS and 1 μg/ml bovine Insulin (Sigma Aldrich), with medium changes every 48 hr. Cells were then stimulated with 1 μM 15-keto-PGE_2 or rosiglitazone (Cayman Chemicals) overnight. Cells were harvested in TRIZOL, RNA isolated and cDNA synthesis performed with subsequent qPCR for Ap2 and Angptl4 as described above.

Genotyping of $HPGD^{fl/fl}$ Mice

For genotyping, ear clippings were digested in DirectPCR Tail Lysis Reagent (Peqlab) with 0.2 mg/ml Proteinase K as per manufacturer's instructions. Genotyping was performed with the MyTaq HS DNA Polymerase (Bioline). Expected band sizes: recombined allele 628 bp; conditional allele 536 bp; wild-type allele 473 bp. Primer sequences are listed in Table S7.

Analysis of HPGD Expression in Immune Cell Datasets

Publicly available datasets from http://Immgen.org and http://Nextbio.org were analyzed for HPGD expression. Normalized data were plotted as expression values.

Cibersort

RNA transcriptome data from peripheral blood cells was analyzed using the CIBERSORT (cell-type identification by estimating relative subsets of RNA transcripts) algorithm (https://cibersort.stanford.edu/) as described previously (Newman et al., 2015) to enumerate immune cell subpopulations. Two publicly available datasets from type 2 diabetes patients with healthy individuals as controls were used (GEO: GSE9006 and EMTAB-1954).

QUANTIFICATION AND STATISTICAL ANALYSIS

Data are represented as mean ± SEM unless otherwise specified. Sample sizes for each experiment are included in the figure legends. Statistical analyses were performed using GraphPad Prism.

DATA AND SOFTWARE AVAILABILITY

The accession numbers for the data generated in this paper are as follows: microarray data can be accessed under GEO: GSE15390, the raw RNA sequencing data has been deposited to GEO with accession number GEO: GSE62579, tiling array data can be accessed under GEO: GSE20995 and VAT RNA-Seq data can be accessed under GEO: GSE123888.